RESEARCH ARTICLE

Key Points:

- Both the liquid and vapor fluxes transfer upward to the freezing front during freeze-thaw process
- The diurnal behavior of thermal vapor flux resulted in the diurnal cycle of soil moisture in region between the evaporation and cold front
- The interactive effect of soil ice and air was found on the spatial and temporal variations of water/vapor transfers

Correspondence to:
L. Yu,
l.yu@utwente.nl

Liquid-Vapor-Air Flow in the Frozen Soil

Lianyu Yu[1] (ID)**, Yijian Zeng[1]** (ID)**, Jun Wen[2]** (ID)**, and Zhongbo Su[1]** (ID)

[1]Faculty of Geo-information and Earth Observation (ITC), University of Twente, Enschede, Netherlands, [2]College of Atmospheric Sciences, the Plateau Atmosphere and Environment Key Laboratory of Sichuan Province, Chengdu University of Information Technology, Chengdu, China

Abstract Accurate representing freeze-thaw (FT) process is of great importance in cold region hydrology and climate studies. With the STEMMUS-FT model (Simultaneous Transfer of Energy, Mass and Momentum in Unsaturated Soil), we investigated the coupled water and heat transfer in the variably saturated frozen soil and the mechanisms of water phase change along with both evaporation and FT process, at a typical meadow ecosystem on the Tibetan Plateau. The STEMMUS-FT showed its capability of depicting the simultaneous movement of soil moisture and heat flow in frozen soil. The comparison of different parameterizations of soil thermal conductivity indicated that the de Vries parameterization performed better than others in reproducing the hydrothermal dynamics of frozen soils. The analysis of water/vapor fluxes indicated that both the liquid water and vapor fluxes move upward to the freezing front and highlighted the crucial role of vapor flow during soil FT cycles as it connects the water/vapor transfer beneath the freezing front and above the evaporation front. The liquid/vapor advective fluxes make a negligible contribution to the total mass transfer. Nevertheless, the interactive effect of soil ice and air can be found on the spatial and temporal variations of advective fluxes in frozen soils.

1. Introduction

Cold region hydrology is of significant importance to global climate change studies (Cheng & Wu, 2007; Ding et al., 2017; Hinzman et al., 2005; Yang et al., 2014). For instance, soil freeze-thaw (hereafter as FT) will sharply disturb the thermodynamic equilibrium system and release/absorb large amount of latent heat (Boike et al., 1998; Li & Koike, 2003). This will further mediate the exchange of water and energy flux between the surface and atmosphere (Viterbo et al., 1999). Moreover, the degradation of permafrost will release carbon stored in the frozen soils and generate the positive feedback on the global warming (Burke et al., 2013; Schaefer et al., 2014). Thus, understanding and representing the underlying physics of FT process are of great interest among scientists.

Large modeling efforts have been made to understand the FT process in cold region as reviewed by Kurylyk and Watanabe (2013). Most of these FT models, however, differed not only in the physics representing the FT process but also in many other ways: for example, numerical discretizations, diagnostic variables, and application in different regions (Bao et al., 2016; Li & Koike, 2003; Su et al., 2013; Wang et al., 2010; Wang et al., 2017; Zhang et al., 2008; Zhang et al., 2010; Zhang et al., 2013). These factors render the intercomparison results difficult to be interpreted and hard to identify the underlying difference among the various FT parameterizations.

Moreover, soil ice, liquid water, and water vapor dynamically coexist in the frozen soil pores; the phase change of soil water usually happens along with large amount of latent heat flux (Boike et al., 1998; Li & Koike, 2003). Soil water and heat transfer are strongly coupled during FT process; neglecting this coupling process in most of the current models limited their capability of accurate description of soil FT physics (Endrizzi et al., 2014; Zhang et al., 2007; Zheng, van der Velde, et al., 2017).

The water vapor flow, which has been proved to be of great importance in water and heat transfer of dry soils (Bittelli et al., 2008; Yu et al., 2016; Zeng, Su, et al., 2009; Zeng, Wan, et al., 2009), recently have been taken into account by land surface models (LSMs; Garcia Gonzalez et al., 2012). Similar to the drying soils, vapor flow also plays an important role in frozen soils. Experimental evidence have demonstrated that vapor flow is essential in ice formation and frost heave (Eigenbrod & Kennepohl, 1996; Zhang et al., 2016). Dandar et al. (2017) found that the vapor diffusion process can affect not only the water balance but also the energy balance
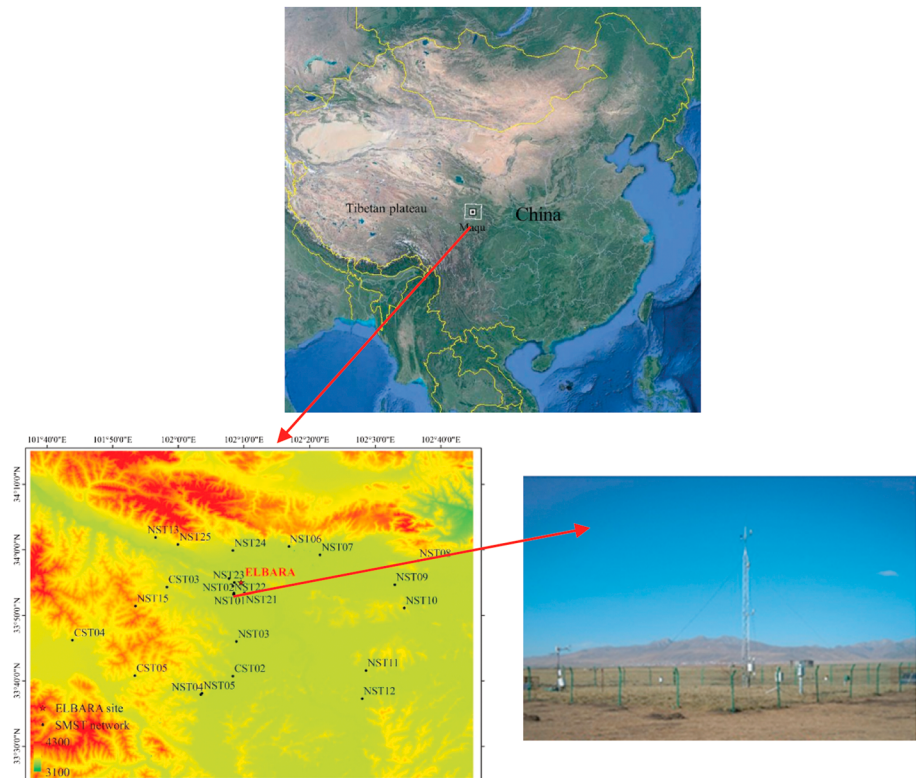
Figure 1. Location of Maqu soil moisture and soil temperature (SMST) monitoring networks. The bottom right figure is the micrometeorological site. Adapted from Zheng, Wang, et al. (2017).

component. The relative contributions of different fluxes and underlying mechanism of water and vapor transfer in drying soils have been widely reported (Boulet et al., 1997; Grifoll et al., 2005; Saito et al., 2006; Scanlon & Milly, 1994), while little attention has been devoted to such kind of research in terms of frozen soils. Dry air is also one independent component in soil pores. It can significantly retard the infiltration (Prunty & Bell, 2007; Touma & Vauclin, 1986), enhance the evaporation after irrigation (Zeng et al., 2011a, 2011b; Zeng & Su, 2013b), and cause the convective heat transfer (Wicky & Hauck, 2017). However, how and to what extent the air component affects the soil water and vapor transfer in frozen soils remain unclear.

In this paper, we conducted an intercomparison of different FT parameterizations based on a common fully coupled water and heat modeling framework (STEMMUS-FT, Simultaneous Transfer of Energy, Mass and Momentum in Unsaturated Soil with Freeze-Thaw). On the basis of STEMMUS-FT with the reliable hydrothermal parameterization, we concentrated our research on the investigation of the mechanism of water, vapor, and air flow of FT processes. Section 2 introduces the experimental site and the STEMMUS-FT governing equations and underlying physics, the design of numerical experiments for intercomparing different FT parameterizations, and the soil freezing curves as deployed. Section 3 presents the intercomparison results of different FT parameterizations, which identified the best representative schemes for the Tibetan site under investigation. Different mechanisms of water and vapor transfer in frozen soils were analyzed. Section 4 discusses the effect of soil ice and the role of vapor and air flow in the frozen soil. The study was concluded in section 5.

2. Experiment Site and Methodology

2.1. Experiment Site

The Maqu soil moisture and soil temperature (SMST) monitoring network (Dente et al., 2012; Su et al., 2011; Zeng et al., 2016) was set up on the north-eastern fringe of the Tibetan Plateau (33°30′–34°15′N, 101°38′–102°45′E; Figure 1). The monitoring network spans an area of approximately 40 km × 80 km, and the

elevation ranges from 3,200 to 4,200 m above sea level. Referring to the updated Köppen-Geiger climate Classification System, it can be characterized as a wet and cold climate, with dry winters and rainy summers. The mean annual air temperature is 1.28 °C, and the mean air temperatures of the coldest month (January) and warmest month (July) are about −10 and 11.7 °C, respectively. Land cover in this region is dominated by alpine meadows with heights varying from 5 to 15 cm throughout the growing season. The general soil types are sandy loam, silt loam, and organic soil with an average 39.7% sand, 8.08% clay, and a maximum of 18.3% organic matter (Dente et al., 2012; Zheng et al., 2015; Zhao et al., 2017; Zhao et al., 2018). The groundwater level is about 8.5–12.0 m below the soil surface.

In Maqu site, SMST profiles are automatically measured at a 15-min interval by 5TM ECH$_2$O probes (Decagon Devices, Inc., USA) installed at the following depths: 5, 10, 20, 40, 80, and 160 cm. The micrometeorological observing system includes a 20 m planetary boundary layer tower providing wind speed and direction, air humidity and temperature measurements at five heights above ground, and an eddy-covariance system installed for measuring the turbulent heat fluxes. Instrumentations for measuring four radiation components (i.e., upward and downward shortwave and longwave radiations), air pressure, and liquid precipitation are also deployed. Detailed description of the measurements and observations can refer to Dente et al. (2012) and Zheng et al. (2014).

2.2. STEMMUS-FT Model

The STEMMUS, detailed in Zeng et al. (2011a, 2011b), Zeng (2013), and Zeng & Su (2013a), taking into account the soil FT process (STEMMUS-FT) was developed. The details of governing equations are given below.

2.2.1. Soil Water Transfer

$$\frac{\partial}{\partial t}(\rho_L \theta_L + \rho_V \theta_V + \rho_i \theta_i) = -\frac{\partial}{\partial z}(q_{Lh} + q_{LT} + q_{La} + q_{Vh} + q_{VT} + q_{Va}) - S$$

$$= \rho_L \frac{\partial}{\partial z}\left[K\left(\frac{\partial h}{\partial z} + 1\right) + D_{TD}\frac{\partial T}{\partial z} + \frac{K}{\gamma_w}\frac{\partial P_g}{\partial z}\right] + \frac{\partial}{\partial z}\left[D_{Vh}\frac{\partial h}{\partial z} + D_{VT}\frac{\partial T}{\partial z} + D_{Va}\frac{\partial P_g}{\partial z}\right] - S \quad (1)$$

where ρ_L, ρ_V, and ρ_i (kg/m^3) are the density of liquid water, water vapor, and ice, respectively; θ_L, θ_V, and θ_i (m^3/m^3) are the volumetric water content (liquid, vapor, and ice, respectively); z (m) is the vertical space coordinate (positive upwards); and S (s^{-1}) is the sink term for the root water extraction. K (m/s^1) is hydraulic conductivity, h (m) is the pressure head, T (°C) is the soil temperature, and P_g (Pa) is the mixed pore-air pressure. The γ_W (kg $\cdot$ m^{-2} $\cdot$ s^{-2}) is the specific weight of water. D_{TD} (kg $\cdot$ m^{-1} $\cdot$ s^{-1} $\cdot$ °C^{-1}) is the transport coefficient for adsorbed liquid flow due to temperature gradient, D_{Vh} (kg $\cdot$ m^{-2} $\cdot$ s^{-1}) is the isothermal vapor conductivity, and D_{VT} (kg $\cdot$ m^{-1} $\cdot$ s^{-1} $\cdot$ °C^{-1}) is the thermal vapor diffusion coefficient. D_{Va} is the advective vapor transfer coefficient (Zeng et al., 2011a, 2011b). The q_{Lh}, q_{LT}, and q_{La} (kg $\cdot$ m^{-2} $\cdot$ s^{-1}) are the liquid water fluxes driven by the gradient of matric potential $\frac{\partial h}{\partial z}$, temperature $\frac{\partial T}{\partial z}$, and air pressure $\frac{\partial P_g}{\partial z}$, respectively. The q_{Vh}, q_{VT}, and q_{Va} (kg $\cdot$ m^{-2} $\cdot$ s^{-1}) are the water vapor fluxes driven by the gradient of matric potential $\frac{\partial h}{\partial z}$, temperature $\frac{\partial T}{\partial z}$, and air pressure $\frac{\partial P_g}{\partial z}$, respectively.

2.2.2. Dry Air Transfer

$$\frac{\partial}{\partial t}[\varepsilon \rho_{da}(S_a + H_c S_L)] = \frac{\partial}{\partial z}\left[D_e \frac{\partial \rho_{da}}{\partial z} + \rho_{da}\frac{S_a K_g}{\mu_a}\frac{\partial P_g}{\partial z} - H_c \rho_{da}\frac{q_L}{\rho_L} + (\theta_a D_{Vg})\frac{\partial \rho_{da}}{\partial z}\right] \quad (2)$$

where ε is the porosity, ρ_{da} (kg/m^3) is the density of dry air, S_a ($=1 - S_L$) is the degree of air saturation in the soil, S_L ($=\theta_L/\varepsilon$) is the degree of saturation in the soil, H_c is Henry's constant, D_e (m^2/s) is the molecular diffusivity of water vapor in soil, K_g (m^2) is the intrinsic air permeability, μ_a (kg $\cdot$ m^{-2} $\cdot$ s^{-1}) is the air viscosity, q_L (kg $\cdot$ m^{-2} $\cdot$ s^{-1}) is the liquid water flux, θ_a ($=\theta_V$) is the volumetric fraction of dry air in the soil, and D_{Vg} (m^2/s) is the gas phase longitudinal dispersion coefficient (Zeng et al., 2011a, 2011b).

2.2.3. Energy Transfer

$$\frac{\partial}{\partial t}[(\rho_s \theta_s C_s + \rho_L \theta_L C_L + \rho_V \theta_V C_V + \rho_{da}\theta_a C_a + \rho_i \theta_i C_i)(T - T_r) + \rho_V \theta_V L_0 - \rho_i \theta_i L_f] - \rho_L W \frac{\partial \theta_L}{\partial t}$$

$$= \frac{\partial}{\partial z}\left(\lambda_{eff}\frac{\partial T}{\partial z}\right) - \frac{\partial}{\partial z}[q_L C_L(T - T_r) + q_V(L_0 + C_V(T - T_r)) + q_a C_a(T - T_r)] - C_L S(T - T_r) \quad (3)$$
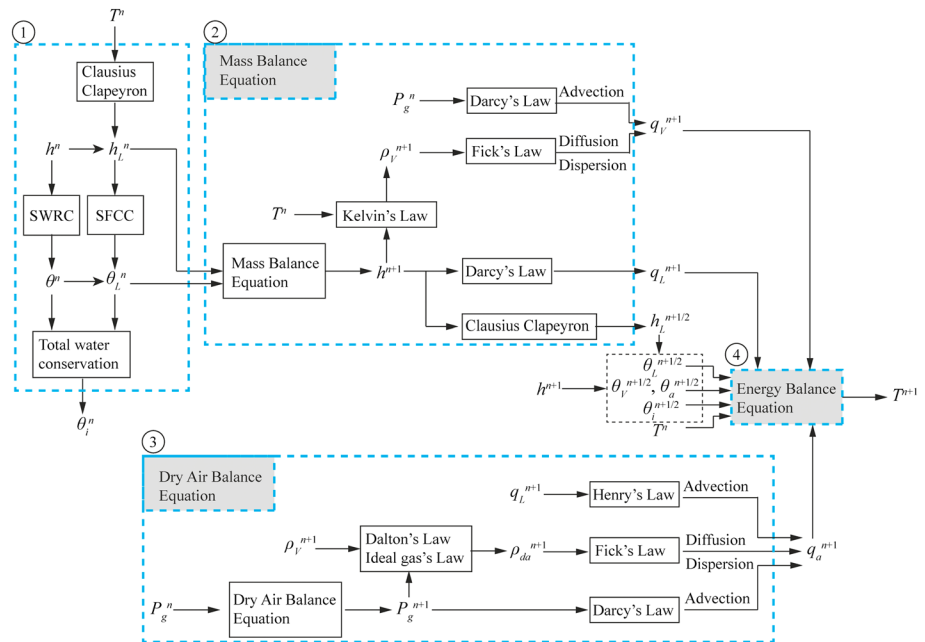
Figure 2. The underlying physics and calculation procedure of STEMMUS-FT expressed within one time step. n is the time at the beginning of the time step, $n + 1$ is the time at the end. The variables with the superscript ($n + 1/2$) are the intermediate values.

where C_s, C_L, C_V, C_a, and C_i ($J \cdot kg^{-1} \cdot °C^{-1}$) are the specific heat capacities of solids, liquid, water vapor, dry air, and ice, respectively; ρ_s (kg/m^3) is the density of solids; θ_s is the volumetric fraction of solids in the soil; T_r (°C) is the reference temperature; L_0 (J/kg) is the latent heat of vaporization of water at temperature T_r; L_f (J/kg) is the latent heat of fusion; W (J/kg) is the differential heat of wetting (the amount of heat released when a small amount of free water is added to the soil matrix); and λ_{eff} ($W \cdot m^{-1} \cdot °C^{-1}$) is the effective thermal conductivity of the soil; q_L, q_V, and q_a ($kg \cdot m^{-2} \cdot s^{-1}$) are the liquid, vapor water flux, and dry air flux.

2.2.4. Underlying Physics and Calculation Procedure of STEMMUS-FT

2.2.4.1. Underlying Physics of STEMMUS-FT

When soil water starts freezing, soil liquid water, ice, vapor, and gas coexist in soil pores. A new thermodynamic equilibrium system will be reached and can be described by the Clausius Clapeyron equation (Figure 2). In combination with soil freezing characteristic curve (SFCC), the storage variation of soil water can be partitioned into the variation of liquid water content θ_L and ice content θ_i, and then vapor content θ_V.

With regard to a unit volume of soil, the change of water mass storage with time can be attributed to the change of liquid/vapor fluxes and the root water uptake S (equation (1)). The fluxes, in the right-hand side of equation (1), can be generalized as the sum of liquid and vapor fluxes. The liquid water transfer is expressed by a general form of Darcy's flow $\left(-\rho_L K \frac{\partial\left(h+\frac{P_g}{\gamma_w}+z\right)}{\partial z}\right)$. According to Groenevelt and Kay (1974), the other source of liquid flow is induced by the effect of the heat of wetting on the pressure field $\left(-\rho_L D_{TD}\frac{\partial T}{\partial z}\right)$.

The vapor flow is assumed to be induced in three ways: (i) the diffusive transfer (Fick's law), driven by a vapor pressure gradient $\left(-D_V\frac{\partial\rho_V}{\partial z}\right)$, (ii) the dispersive transfer due to the longitudinal dispersivity (Fick's law, $-\theta_V D_{Vg}\frac{\partial\rho_V}{\partial z}$), and (iii) the advective transfer, as part of the bulk flow of air $\left(\rho_V\frac{q_a}{\rho_{da}}\right)$. As the vapor density is a function of temperature T and matric potential h (Kelvin's law, equation (A21)), the diffusive and dispersive vapor flux can be further partitioned into isothermal vapor flux, driven by the matric potential gradient $\left(D_{Vh}\frac{\partial h}{\partial z}\right)$, and the thermal vapor flux, driven by the temperature gradient $\left(D_{VT}\frac{\partial T}{\partial z}\right)$. The advective vapor flux, driven by the air pressure gradient, can be expressed as $\left(D_{Va}\frac{\partial P_g}{\partial z}\right)$ in equation (1).

Dry air transfer in soil includes four components (equation (2)): (1) the diffusive flux (Fick's law) $D_e \frac{\partial \rho_{da}}{\partial z}$, driven by dry air density gradient; (2) the advective flux (Darcy's law, $\rho_{da} \frac{S_a K_g}{\mu_a} \frac{\partial P_g}{\partial z}$), driven by the air pressure gradient; (3) the dispersive flux (Fick's law, $\left(\theta_a D_{Vg}\right) \frac{\partial \rho_{da}}{\partial z}$); and (4) the advective flux due to the dissolved air (Henry's law, $H_c \rho_{da} \frac{q_L}{\rho_L}$). According to Dalton's law of partial pressure, the mix soil air pressure P_g is the sum of the dry air pressure and water vapor pressure. Considering dry air as an ideal gas, the dry air density, ρ_{da}, can be expressed as the function of air pressure P_g, water vapor density ρ_V, thus the function of three state variables (h, T, P_g; see equations (A22) and (A23)).

Heat transfer in soils includes conduction and convection. The conductive heat transfer contains contributions from liquid, solid, gas, and ice $\left(\lambda_{eff} \frac{\partial T}{\partial z}\right)$. The convective heat is transferred by liquid flux $-C_L q_L(T - T_r)$, $-C_L S(T - T_r)$, vapor flux $-[L_0 q_V + C_V q_V(T - T_r)]$, and air flow $q_a C_a(T - T_r)$. The heat storage in soil, the left-hand side of equation (3), includes the bulk volumetric heat content $(\rho_s \theta_s C_s + \rho_L \theta_L C_L + \rho_V \theta_V C_V + \rho_i \theta_i C_i)(T - T_r)$, the latent heat of vaporization $(\rho_V \theta_V L_0)$, the latent heat of freezing/thawing $(-\rho_i \theta_i L_f)$, and a source term associated with the exothermic process of wetting of a porous medium (integral heat of wetting) $\left(-\rho_L W \frac{\partial \theta_L}{\partial t}\right)$.

2.2.4.2. Calculation Procedure of STEMMUS-FT

The mutual dependence of soil temperature and water content makes frozen soils a complicated thermo-dynamic equilibrium system. The freezing effect explicitly considered in STEMMUS-FT includes three parts: (i) the blocking effect on conductivities (see Appendix (A.2.)), (ii) thermal effect on soil thermal capacity/conductivity (see Appendix (A.3.)), and (iii) the release/absorption of latent heat flux during water phase change. The calculation procedure of STEMMUS-FT can be summarized as below (Figure 2).

Step 1. Partition of the soil mass storage

First, applying the Clausius Clapeyron equation, soil temperature T at time step n was utilized to achieve the initial soil freezing water potential. Given the prefreezing water matric potential h and liquid water matric potential h_L, the SFCC and SWRC are applied to obtain prefreezing water content θ and liquid water content θ_L. Then the soil ice content θ_i can be derived via total water conservation equation considering the difference in the density between liquid and ice water. The volumetric fraction of soil vapor θ_V in soil pores is the difference of soil porosity and the total water content.

Step 2. Solving the mass balance equation

Taking the soil mass storage variables and matric potentials as inputs, we can solve the mass balance equation successfully. Then a new matric potential can be achieved. Applying Darcy's law with consideration of the blocking effect of soil ice on the hydraulic conductivity, we can get liquid water flux q_L. The liquid water matric potential can be updated by applying Clausius Clapeyron equation. Applying the Kelvin's law (equation (A21)), we can update the vapor density ρ_V at the end of time step. Then the dispersive and diffusive vapor fluxes are possible to be calculated according to Fick's law. Another component of vapor flux is considered as part of the bulk flow of air, which is driven by the air pressure according to Darcy's law.

Step 3. Solving the dry air balance equation.

When considering soil dry air as an independent component in soil pores, the dry air balance equation is utilized, whose solution provides the new air pressure P_g^{n+1}. Applying Dalton's law, air pressure can be partitioned into vapor pressure and dry air pressure. Given the updated vapor density, the dry air density can be expressed as the function of air pressure, and vapor density (equations (A22) and (A23)). Applying Fick's law, we can calculate the diffusive and dispersive components of dry air flux. Applying Darcy's law, the advective flux is derived from the air pressure. To maintain the mechanical and chemical equilibrium, a certain amount of air will dissolve into liquid; such effect is described by Henry's law. Finally, we can achieve the dry air flux q_a by the sum of the aforementioned effects.

Step 4. Solving the energy balance equation

Given the inputs, updated values of liquid water flux q_L^{n+1}, water vapor flux q_V^{n+1}, soil liquid water content $\theta_L^{n+1/2}$, vapor content $\theta_V^{n+1/2}$, ice content $\theta_i^{n+1/2}$, and dry air flux q_a^{n+1}, we can update the thermal parameters, calculate the latent heat of water phase change, then solve the energy balance equation. A successful estimate of soil temperature will be obtained, which can be used as input for the next time step.

Table 1
Different Model Parameterizations for Frozen Soil

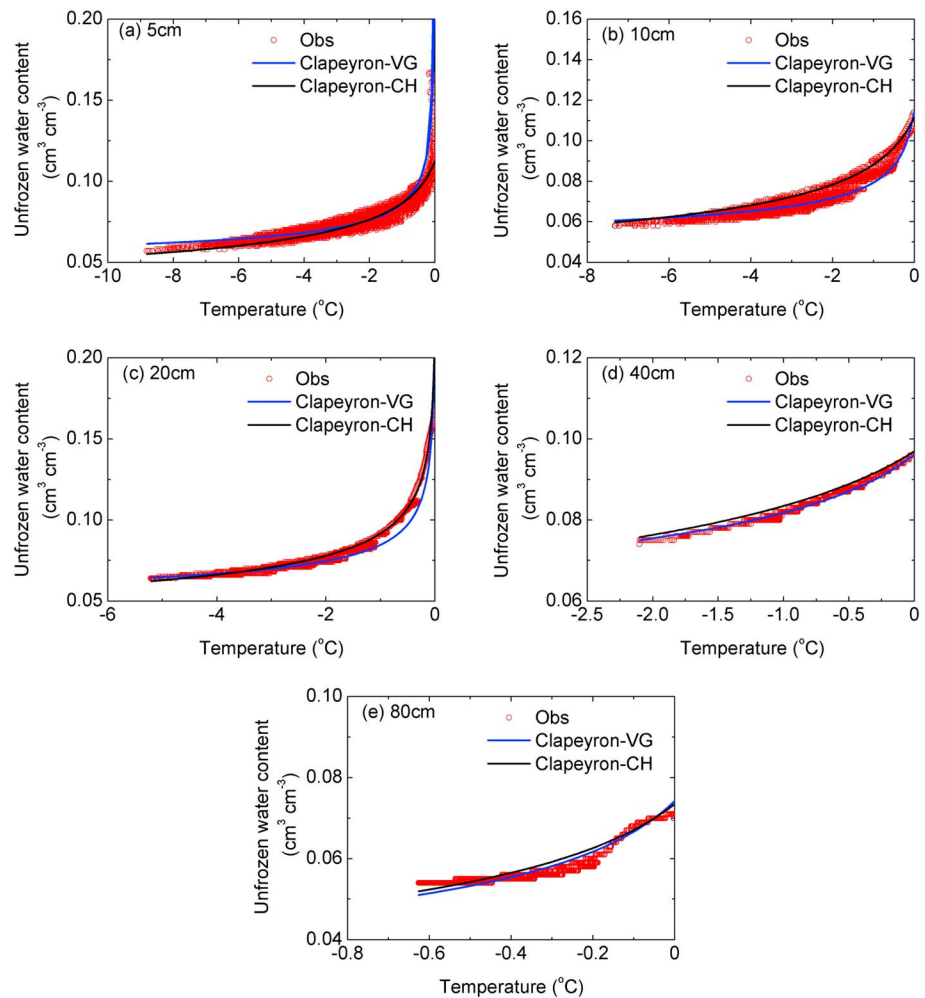| Model	Unfrozen water content	Hydraulic conductivity K	Heat conductivity	Soil water and heat transfer	Reference
Noah-MP	SFCC (Clapeyron + Clapp and Hornberger)[a]	Clapp and Hornberger + ice correction coefficient	Johansen method	uncoupled	Yang et al. (2011)
CLM 4.5	SFCC (Clapeyron + Clapp and Hornberger)	Clapp and Hornberger + ice correction coefficient	Johansen method	uncoupled	Oleson et al. (2013)
SHAW	SFCC (Clapeyron + Brooks-Corey)	Clapp and Hornberger, reduced linearly with ice content	de Vires method	coupled	Flerchinger and Saxton (1989)
COUP	Available energy for phase change	van Genuchten + impedance factor	Kersten method	coupled	Jansson (2012)
CLASS	Available energy for phase change	Clapp and Hornberger + ice correction coefficient	Johansen method	coupled	Verseghy (2009)
HTESSEL	SFCC (empirical function of soil temperature)	Weighted values between unfrozen and frozen hydraulic conductivity	Johansen method	uncoupled	Viterbo et al. (1999)
HYDRUS	SFCC (Clapeyron + van Genuchten)	van Genuchten + impedance factor	Modified Campbell method	coupled	Hansson et al. (2004)
CoLM	SFCC (Clapeyron + Clapp and Hornberger)	Clapp and Hornberger + ice correction	Johansen method	uncoupled	Dai et al. (2001)

Figure 3. Observed and simulated unfrozen water content under subfreezing soil temperature using two SFCC parameterizations at different soil layers (5, 10, 20, 40, and 80 cm). Clapeyron-VG and Clapeyron-CH represent the SFCC using van Genuchten (van Genuchten, 1980) and Clapp and Hornberger (Clapp & Hornberger, 1978) method, respectively.
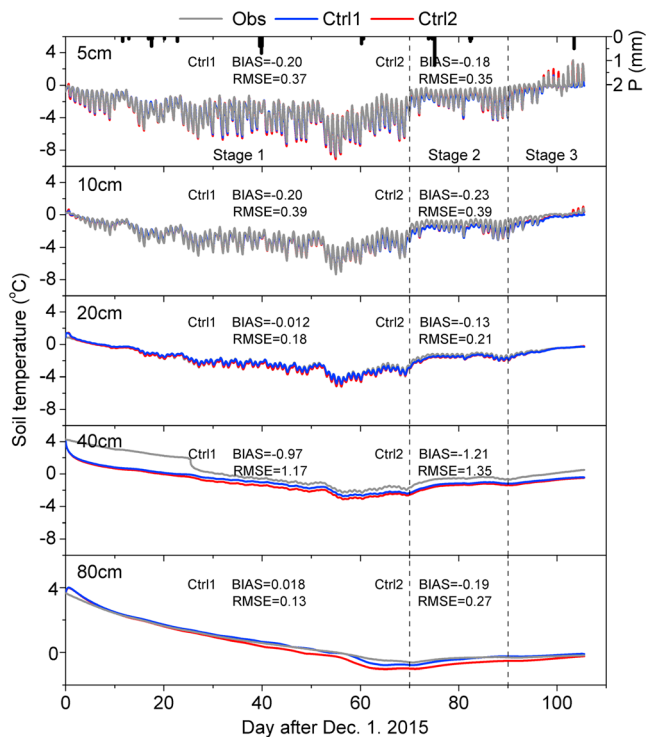
Figure 4. Comparison of observed and simulated soil temperature at different soil layers using different parameterizations of unfrozen water content and hydraulic conductivity (Ctrl1-Ctrl2).

Note that the effect of snow accumulation and ablation was not considered in the current version of STEMMUS-FT model. In our further development of the model, we will incorporate such effect in a more realistic and physical way (e.g., Boone & Etchevers, 2001; Ding et al., 2017; Koren et al., 1999; Tarboton & Luce, 1996; Wang et al., 2017).

2.3. FT Parameterizations

The water and heat flow during FT processes can be generally characterized by three main sets of parameters: unfrozen water content, hydraulic conductivity, and heat capacity/conductivity. Among the commonly used models, two categories of method to estimate unfrozen water content were employed: (i) water change as from water to ice is calculated by the available heat energy for such a phase change process (Jansson, 2012). The fixed freezing point is assumed in these schemes and thus it simplifies the physical process of FT; (ii) soil freezing depression theory and soil water retention curve are combined to derive the SFCC, which is a function of soil temperature to estimate the unfrozen water content (Flerchinger & Saxton, 1989; Hansson et al., 2004). Due to the high sensitivity to the calibration of related soil parameters, the empirical equations-based frozen soil parameterizations (e.g., Li & Koike, 2003; Wang et al., 2009; Wang et al., 2010) were not considered in this study.

The effect of ice presence in soil pores on the hydraulic conductivity is generally characterized by a correction coefficient, which is a function of ice content (Hansson et al., 2004; Taylor & Luthin, 1978). The calculation of heat conductivity can be divided into three categories: empirical Campbell method (Hansson et al., 2004), Johansen method (Johansen, 1975), and de Vires method (de Vries, 1963). Due to the necessity in the calibration of parameters, the empirical Campbell method is complicated and rarely employed in LSMs and thus not discussed in the current context, while other variations of Johansen method and de Vries method, in which the parameters are based on soil texture information, that is, Farouki method (Farouki, 1981) and simplified de Vries method (Tian et al., 2016), were further incorporated into STEMMUS-FT. A brief review of the different parameterizations for frozen soil employed in current models is given by Table 1.

The above FT parameterizations are used as constitutive equations for STEMMUS-FT and are detailed in Appendix A and further designed as different numerical experiments in section 2.4.

2.4. Design of Numerical Experiments

To assess the effect of different hydraulic parameterizations on the performance of STEMMUS-FT model, two control experiments (Ctrl1 and Ctrl2) were designed, in which van Genuchten and Clapp and Hornberger hydraulic schemes were employed respectively, with de Vries method for the heat conductivity. On the basis of two control experiments, the performance of STEMMUS-FT with three other thermal parameterizations was further investigated (i.e., EXP1 for Farouki method, EXP2 for Simplified de Vries method, and EXP3 for Johansen method).

A data set collected from 1 December 2015 to 15 March 2016 at Maqu SMST site was employed to run and evaluate all the numerical experiments. Soil moisture and temperature at various depths are utilized to initialize and to validate STEMMUS-FT model. Land surface latent heat flux is employed to investigate the model performance and further to testify the underlying physics of soil water, vapor, and air transfer in the frozen soil. The average feature of soil properties are listed in Table 3. The type of vegetation is grassland, which will be in low activity during frozen periods. Thus, the assumption that there is no transpiration when soil temperature drops below 0 °C was adopted (Kroes et al., 2009). Refer to Zheng (2015) and Zheng et al. (2015) for further details of the vegetation and soil parameters.

Table 2
Numerical Experiment Designs to Assess the Different FT Parameterizations

Experiment		Unfrozen water content		Hydraulic conductivity		Heat conductivity			
		Clapeyron + VG	Clapeyron + CH	VG	CH	D63	F81	T16	J75
Ctrl1		√		√		√			
Ctrl2			√		√	√			
Ctrl1	EXP1	√		√			√		
	EXP2	√		√				√	
	EXP3	√		√					√
Ctrl2	EXP1		√		√		√		
	EXP2		√		√			√	
	EXP3		√		√				√

Note. VG, van Genuchten (van Genuchten, 1980; equations (A1)–(A4)); CH, Clapp and Hornberger (Clapp & Hornberger, 1978; equation (A5)); heat conductivity: J75, Johansen thermal conductivity method (Johansen, 1975; equations (A9)) to (A13a) and (A13b)); F81, Farouki method (Farouki, 1981; equation (A14)); D63, de Vries method (de Vries, 1963; equations (A15)–(A17)); T16, Simplified De Vries method (Tian et al., 2016; equations (A18)–(A20)).

2.5. SFCC

In order to obtain unfrozen water content, the potential-freezing point depression theory (Dall'Amico, 2010; Koopmans & Miller, 1966) and the reversion of two water retention equations were combined to characterize SFCC, that is, the relation between unfrozen water content and subfreezing temperature. In situ measurements of the liquid water contents for the subzero temperatures at soil depths of 5, 10, 20, 40, and 80 cm were used to fit the SFCCs.

Figure 3 shows the measured and estimated unfrozen water content with two SFCC parameterizations (equations (A2) and (A5)). Both method can capture the dependence of unfrozen water content on soil temperature at different soil depths. Due to the multiple freezing/thawing cycles, the relationships of unfrozen water content and soil temperature are not constrained along with one single SFCC but with certain range (e.g., see observation data in Figures 3a–3c), which indicates the hysteresis effect. It can also be found in Figure 3e that when liquid water content approaches the residual water content (~0.05 cm^3/cm^3), both types of SFCCs fail to capture the relationship between liquid water content and soil temperature.

3. Results

3.1. Assessment of Soil Hydraulic Parameterizations

Figure 4 shows the comparison of soil temperature simulated using two hydraulic schemes (Ctrl 1 and Ctrl 2, with D63 for heat conductivity; see Table 2) and observed values at different soil depths. As indicated by Figure 4, FT processes can be separated into three periods: (i) Freezing period. Despite of the daily fluctuation of soil temperature, the trend of soil temperature keeps falling down, and the freezing front extends downward rapidly. (ii) Transition period. The soil temperature is getting warmer and finally stabilized just below the freezing temperature (melting soil ice requires much more energy). The propagation rate of freezing front slows down and keeps stable. (iii) Thawing period. The soil temperature increase above the freezing temperature as enough energy is absorbed at topsoil. Thawing front initializes from topsoil. Following the Fourier heat transfer theory, the trend of soil temperature propagated downward, while the daily variation damped and

Table 3
The Average Values of Soil Texture and Hydraulic Properties at Different Depths

Soil depth (cm)	Clay (%)	Sand (%)	K_s (10^{-6} m/s)	θ_s (cm^3/cm^3)	CH model		VG model		
					ψ_s (m)	b	θ_r (cm^3/cm^3)	α (m^{-1})	n
5–10	9	44.13	1.45	0.5	0.17	4.178	0.035	0.04139	1.332
10–40	10.12	44.27	0.94	0.45	0.17	4.3	0.039	0.04139	1.3618
40–80	5.59	65.55	0.68	0.41	0.1	3.4	0.045	0.075	1.59

Note. VG, van Genuchten (van Genuchten, 1980); CH, Clapp and Hornberger (Clapp & Hornberger, 1978).
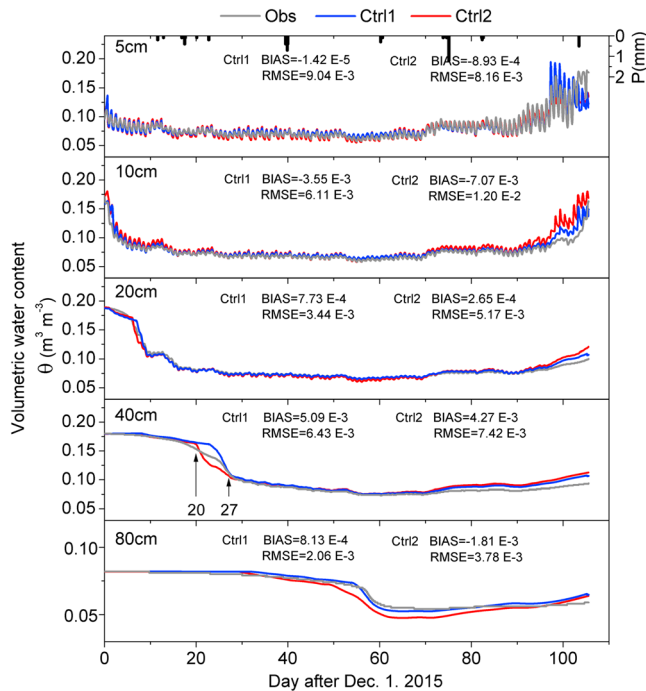
Figure 5. Same as Figure 4 but for volumetric water content.

time lag increased with the increasing soil depths. STEMMUS-FT with both hydraulic schemes can capture very well the diurnal and seasonal variations of soil temperature during the freezing, transition, and thawing period at upper soil layers. At soil depth of 40 cm, the soil temperature was significantly underestimated by STEMMUS-FT model. This may be attributed to the sharply changed soil texture (see Table 3), which has a significant effect on the soil thermal properties. In addition, the observed sharp decrease of soil temperature at 40 cm soil depth around 25 December is abnormal. Whether this observed sharp decrease phenomenon ranged from 2 to 0 °C is an observation error or the misinterpretation of the underlying physics requires further investigation.

Observed soil liquid water content at five soil depths were employed to assess the model performance of STEMMUS-FT with two different hydraulic schemes (Figure 5). For the upper soil layers (5–20 cm), soil liquid water contents were well simulated at freezing period and transition period, while little overestimation was given at the thawing period at soil depth of 10 and 20 cm. During the freezing/thawing transition period, soil suffers from frequent freeze/thaw cycles and the heat exchange (release/absorb latent heat during freezing/thawing process) is significant. The soil hydraulic properties can change observably due to the freeze/thaw cycles (i.e., after the freeze/thaw cycle, the soil hydraulic parameters are not the same as the former ones; Ishikawa et al., 2016; Qi et al., 2006). These make it more difficult to mimic the water and heat transfer during transition periods, especially when the current existing FT models/theories do not consider comprehensively all these effects.

At the soil depth of 40 cm, STEMMUS-FT estimated unfrozen water content agreed well with the measured values except for the rapid freezing period (20–27 December). Soil liquid water content was overestimated and underestimated by the experiment Ctrl1 and Ctrl2, respectively. It can be due to both the soil temperature drop at 40 cm (see Figure 4) and the uncertainties in SFCC models (Figure 3d). The underestimation of soil temperature results in the underestimation of soil liquid water content at 80 cm. While the underestimation of liquid water content for the numerical experiment Ctrl1 is acceptable, such underestimation for the numerical experiment Ctrl2 is obvious from 45th to 80th days after 1 December 2015. The divergence between the two hydraulic schemes enlarged at the rapid freezing period (e.g., 40 cm) and thawing period (e.g., 10 cm), which implicated that the divergence of different hydraulic schemes was highly sensitive to the rapid freezing/thawing process.
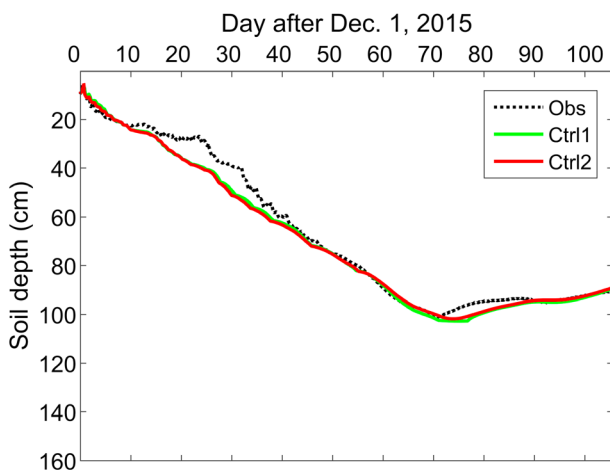
Frost depth, derived from the zero thermal line, was usually employed to characterize the evolution of FT process. As shown in Figure 6, soil water begins to freeze at a relatively high rate, then slows down until 20 December 2015 (i.e., observation in Figure 6), which may be due to the snow insulating effect. The freezing process continues with a high speed and levels off from the 70th days after 1 December 2015. STEMMUS-FT well predicts the dynamic of freezing depth as observed. However, the slowing down of freezing rate during 10–27 December was not fully captured mainly due to (i) the inaccurate "observation" values of frost depth due to the linear interpolation between two soil temperature measurements and (ii) STEMMUS-FT that lacks a detailed representation of snow process on land surface.

3.2. Assessment of Parameterizations of Soil Thermal Conductivity

To understand the effect of multiparameterizations of soil thermal conductivity on modeling the FT process, we investigated the observed and simulated soil freezing front using different thermal schemes (see Table 2). It is to note that the thermal schemes under investigation are all based on the
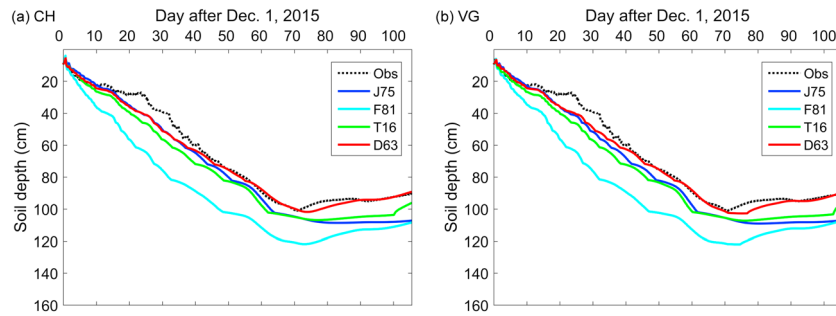

Figure 6. Comparison of observed and simulated soil freezing front using different parameterizations of unfrozen water content and hydraulic conductivity (Ctrl1-Ctrl2).

Figure 7. Comparison of observed and simulated soil freezing front using different parameterizations of thermal conductivity (see Table 2) with (a) Clapp and Hornberger (CH) and (b) van Genuchten (VG) hydraulic schemes.

soil texture information for the inputs. As such, all the input parameters (Table 3) are the same for the designed numerical experiments showed in Table 2. Figure 7 shows that F81 generated the fastest freezing rate than other methods, indicating the highest thermal diffusivity predicted. The J75 and T16 perform better than F81 method; however, a deeper frost depth than the observed values was predicted. D63 method gives the best performance.

3.3. Mechanism of Water and Vapor Transfer in Frozen Soils

After validating the performance of STEMMUS-FT model with different hydro-thermal parameterizations, the simulation results of numerical experiment Ctrl1 were utilized to further investigate the underlying mechanism of water and vapor transfer during FT process.

3.3.1. Freezing Period

Diurnal dynamics of latent heat flux during the rapid freezing period, from eighth to twelfth days after 1 December 2015, is shown as Figure 8a. Although the values are not large, the diurnal variations of latent heat flux was obvious and captured well by the proposed model, with the root-mean-square error, bias, and R^2 values of 1.55E−7, 5.04E−8 g · cm^{-2} · s^{-1}, and 0.80, respectively. To understand the relative contribution of liquid, vapor, and air flow to the total mass flux, the surface latent heat was partitioned into different components as Figures 8b and 8c. According to equation (1), total mass transfer can be separated into liquid water flux driven by temperature q_{LT}, matric potential q_{Lh} and air pressure q_{La}, water vapor flux driven by temperature q_{VT}, matric potential q_{Vh}, and air pressure q_{Va}.

While the downward thermal vapor flux driven by a downward temperature gradient occurred during daytime, there was a comparable amount of upward liquid water flux due to an upward matric potential gradient. The isothermal vapor flux played a dominant role in the total mass flux at topsoil layers when soil is freezing, which is similar to the drying process (Saito et al., 2006). The source for such an upward water vapor flux, however, was not only the isothermal liquid water flux q_{Lh} but also the vapor directly from ice sublimation. Other components, liquid water flux driven by temperature gradient and liquid/vapor water flux driven by air pressure gradient, appeared negligible to the total mass flux during day/nighttime.

Figure 9 shows the vertical flux profiles during the rapid freezing period, which can be classified into different zones as follows. Compared to the thermal/isothermal liquid/vapor fluxes, the air pressure induced liquid/vapor fluxes are relatively small. Thus, we separately presented the vertical variations of liquid/vapor advective fluxes (q_{La}, q_{Va}) in Figure 10.
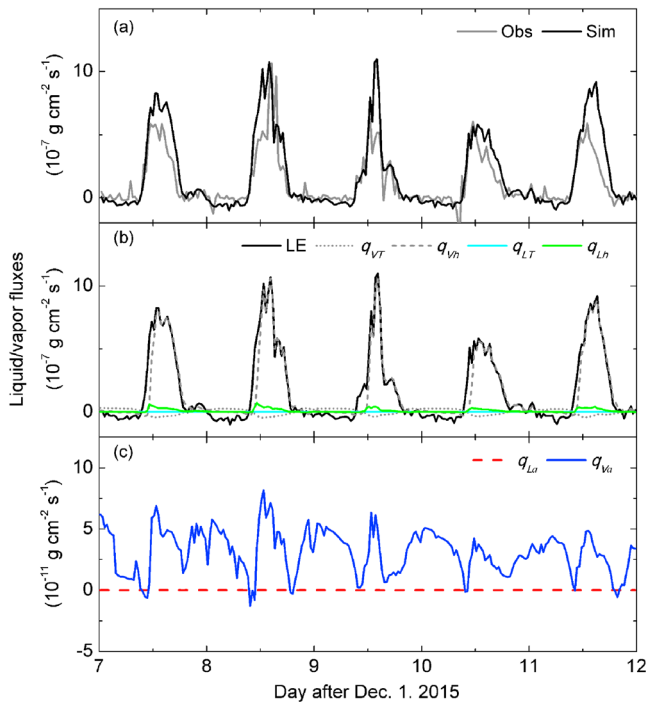

Figure 8. Observed latent heat flux and simulated (a) latent heat flux and (b) surface soil (0.1 cm) thermal and isothermal liquid water and vapor fluxes (LE, q_{VT}, q_{Vh}, q_{LT}, q_{Lh}); (c) surface soil (0.1 cm) advective liquid water and vapor fluxes (q_{La}, q_{Va}) of a typical five-day freezing period (from eighth to twelfth days after 1 December 2015). LE is the latent heat flux, q_{VT} and q_{Vh} are the water vapor fluxes driven by temperature and matric potential gradients, q_{LT} and q_{Lh} are the liquid water fluxes driven by temperature and matric potential gradients, and q_{La} and q_{Va} are the liquid and vapor water fluxes driven by air pressure gradients. Positive/negative values indicate upward/downward fluxes.
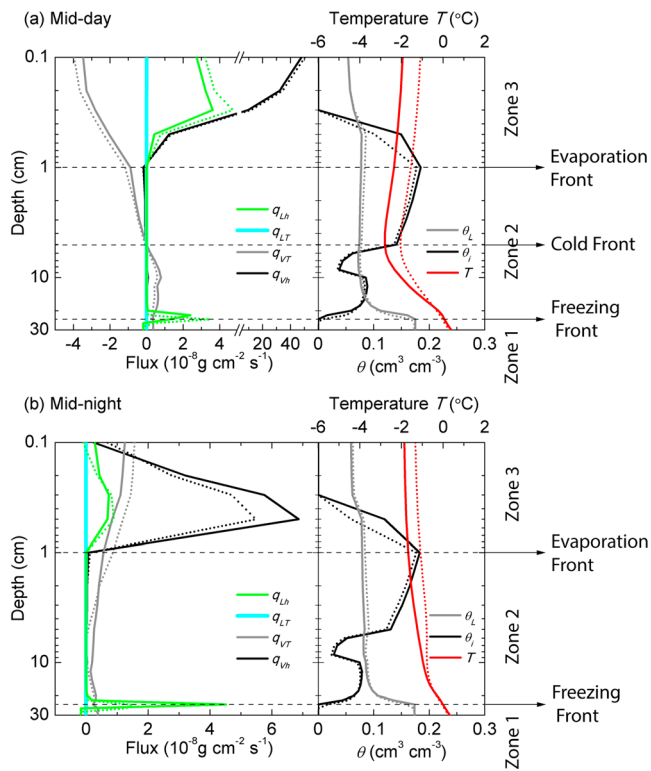
Figure 9. Simulated vertical profiles of the thermal and isothermal liquid water and vapor fluxes, soil ice content at 1200 and 0000 h of a typical freezing period during eleventh and twelfth days after 1 December 2015. Positive/negative values indicate upward/downward fluxes. The solid lines and dotted lines represent the fluxes and soil moisture, temperature, and ice content profile on the eleventh and twelfth days after 1 December 2015, respectively.

1. Zone 1 (region at and below the freezing front)

Observably, an upward transport of liquid water flux q_{Lh} occurred at the freezing front, that is, the soil depth of 22 cm on 11 December, where soil ice diminished (Figure 9a). This movement of liquid water is primarily due to a large upward moisture gradient around the freezing front, with the soil moisture decreased by about 36% (from 0.175 cm^3/cm^3 at soil depth of 24 cm to 0.112 cm^3/cm^3 at soil depth of 20 cm). There was also an observable amount of upward thermal vapor flux q_{VT}, which takes up about 13% of total water flux ($q_{Lh} + q_{VT}$) toward the freezing front. In the region below the freezing front, where the variation of soil moisture was nearly uniform, the isothermal liquid water flux moved downward mainly due to the gravity flow. Note that only the soil depth upper than 30 cm was presented in Figure 9 to concentrate our analysis on the FT process. During the selected typical freezing period, there was no significant effects of FT process on the transport of the water/vapor fluxes in the region below the depth of 30 cm. The water/vapor transfer behavior of this region is similar to the drying process, as reported by Boulet et al. (1997) and Grifoll et al. (2005).

In this region, there was no significant difference in the transfer patterns of soil temperature and moisture gradient induced liquid/vapor fluxes between the daytime and nighttime (Figures 9a and 9b).

2. Zone 2 (frozen region)

Although soil moisture decreased from 0.112 cm^3/cm^3 at soil depth of 20 cm to 0.074 cm^3/cm^3 at soil depth of 5 cm, such a moisture gradient was still not able to overcome the blocking effect of soil ice on the conductivities. Thus, all moisture gradient-driven fluxes (q_{Lh} and q_{Vh}) were negligible in this zone. On the other hand, the variation of temperature was significant. Starting from the freezing temperature at the freezing front (~22 cm in this occasion), soil temperature dropped below −2 °C at a depth of about 5 cm, and the soil depth where the lowest temperature occurred is defined as the cold front. Below the cold front, the thermal vapor flux moved upward due to an upward temperature gradient. Above the cold front, there was a progressive increase of soil temperature with the depth extending to the soil surface, which induced a downward thermal vapor flux during the daytime.

During the nighttime, soil temperature decreased progressively from the freezing front to the soil surface (Figure 9b). Driven by the upward temperature gradient, the thermal vapor flux kept moving upward to the soil surface.

3. Zone 3 (surface evaporation region)

In the top surface region, depth from 1 to 0.1 cm, soil ice began decreasing due to the melting/sublimation effect and was completely diminished at the depth of 0.3 cm. On the other hand, liquid water content varied uniformly from a depth of 1 to 0.5 cm and rapidly decreased by about 31% (from 0.078 to 0.054 cm^3/cm^3) till near the soil surface. Thus, the upward isothermal liquid/vapor fluxes starting from 1 cm can be mainly attributed to the melting/sublimation of soil ice. Once the soil moisture began to decrease, the upward moisture gradient significantly enhanced the transport of liquid and water vapor upward to the soil surface. As partly transformed into vapor flux, there was a noticeable decrease of isothermal liquid flux q_{Lh} near the surface. The source for the evaporation into atmosphere was mainly from the isothermal vapor flux q_{Vh} (see also Figure 8b).

During the night, most of the fluxes near the surface moved upward with relatively low values. Nevertheless, the amount of upward fluxes was larger than the latent heat flux evaporated into the atmosphere. As such, a part of the isothermal liquid and vapor fluxes accumulated around the evaporation front (the depth where
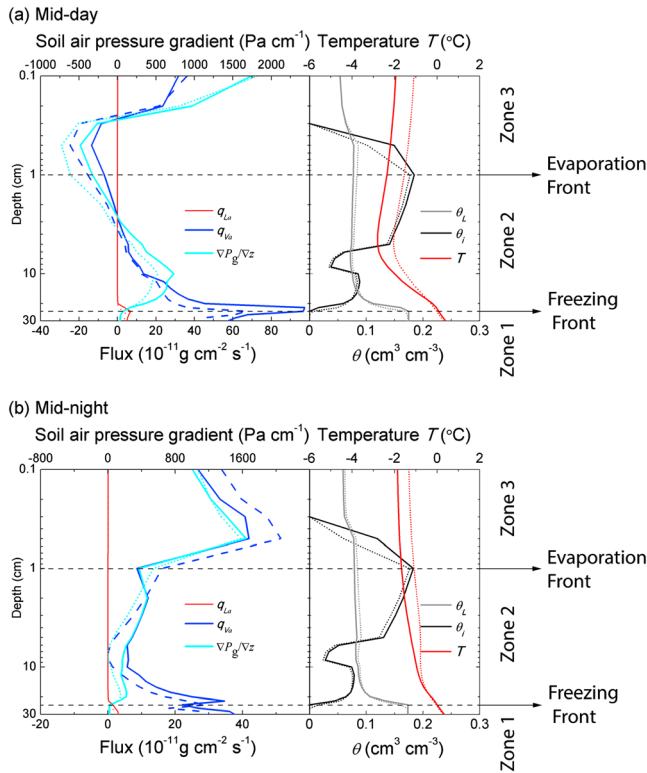
Figure 10. Simulated vertical profiles of the air pressure induced liquid water and vapor fluxes, soil air pressure gradient, soil ice content, liquid water content, and soil temperature at 1200 and 0000 h of a typical freezing period during eleventh and twelfth days after 1 December 2015. Positive/negative values indicate upward/downward fluxes. The solid lines and dotted lines represent the fluxes and soil moisture, temperature, and ice content profile on the eleventh and twelfth days after 1 December 2015, respectively.

the isothermal vapor flux starts dominating the total water flux), resulting in an increase of soil moisture. Such a behavior is similar to the drying process reported by Saito et al. (2006).

The diurnal patterns of water and vapor transport of the latter day were similar to that of the previous day aforementioned. Nevertheless, it is worth to be mentioned that the freezing front was deeper on the twelfth day (Figure 9a). As the freezing front propagated, the peak value of upward liquid water flux q_{Lh} moved downward to a depth of 24 cm. The amount of such water flux, influenced by moisture gradient, was comparable to that of the eleventh day. The contribution of temperature gradient induced thermal vapor flux q_{VT} to total water flux was a bit lower than the previous day with a value of 6.7%.

Figure 10 shows the vertical variations of advective liquid/vapor water fluxes of a typical freezing period. Similar to the isothermal liquid/vapor water flux, there was also a certain amount of air pressure gradient-induced liquid/vapor flow accumulating to the freezing front, mainly due to the interactive effect of ice and air pressure. At the upper soil layers, the air pressure gradient-induced liquid water flux was largely decreased as the impendence effect of ice on the soil permeability. At soil surface, in order to equilibrate with the atmospheric pressure, there was an upward gradient of soil air pressure during the daytime. In the frozen region, the gradient of soil air pressure was significantly reduced, mainly due to the increasing surface contact between solid particles and air. Note that there was a negative soil air pressure gradient at soil depth between 0.2 and 3 cm. The vapor flux driven by air pressure gradient diverged at 0.2 cm, while accumulated at 3 cm. The vertical variations of vapor flux at soil layers above the freezing front were of the same to the variations of air pressure gradient.

During the nighttime, soil air pressure gradients were relatively small in the frozen zone, while increased significantly in the evaporation zone. The variation of liquid/vapor advective fluxes changed synchronously with that of soil air pressure gradients along the vertical profile, except for the soil depth around the freezing front. A certain amount of liquid and vapor advective fluxes moved upward to the freezing front, although soil air pressure gradients are negligible. There is an air pressure-induced diurnal vapor circulation at soil depth between 0.2 and 3 cm.
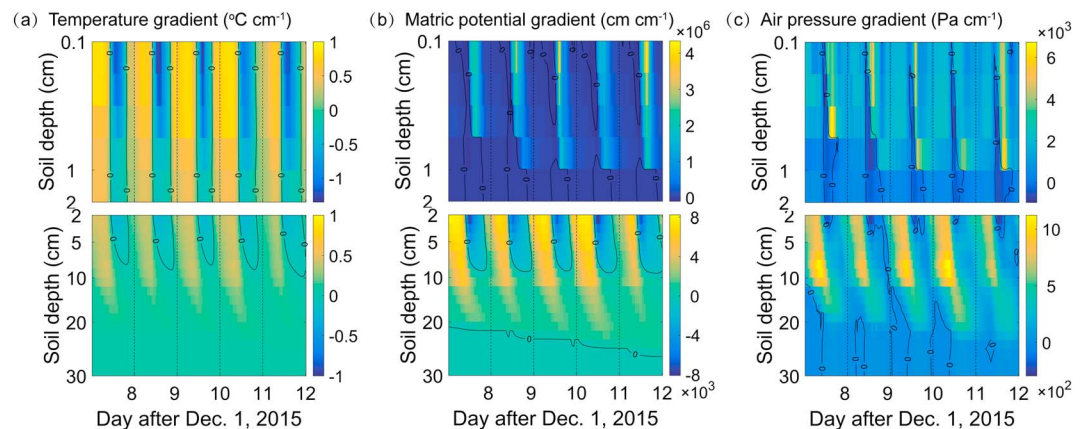

Figure 11. Spatial and temporal variations of (a) temperature gradient, (b) matric potential gradient, and (c) air pressure gradient at surface soil layers (top 2 cm, upper figure) and deeper soil layers (2–30 cm, bottom figure), respectively, of a typical freezing period during eighth and twelfth days after 1 December 2015.
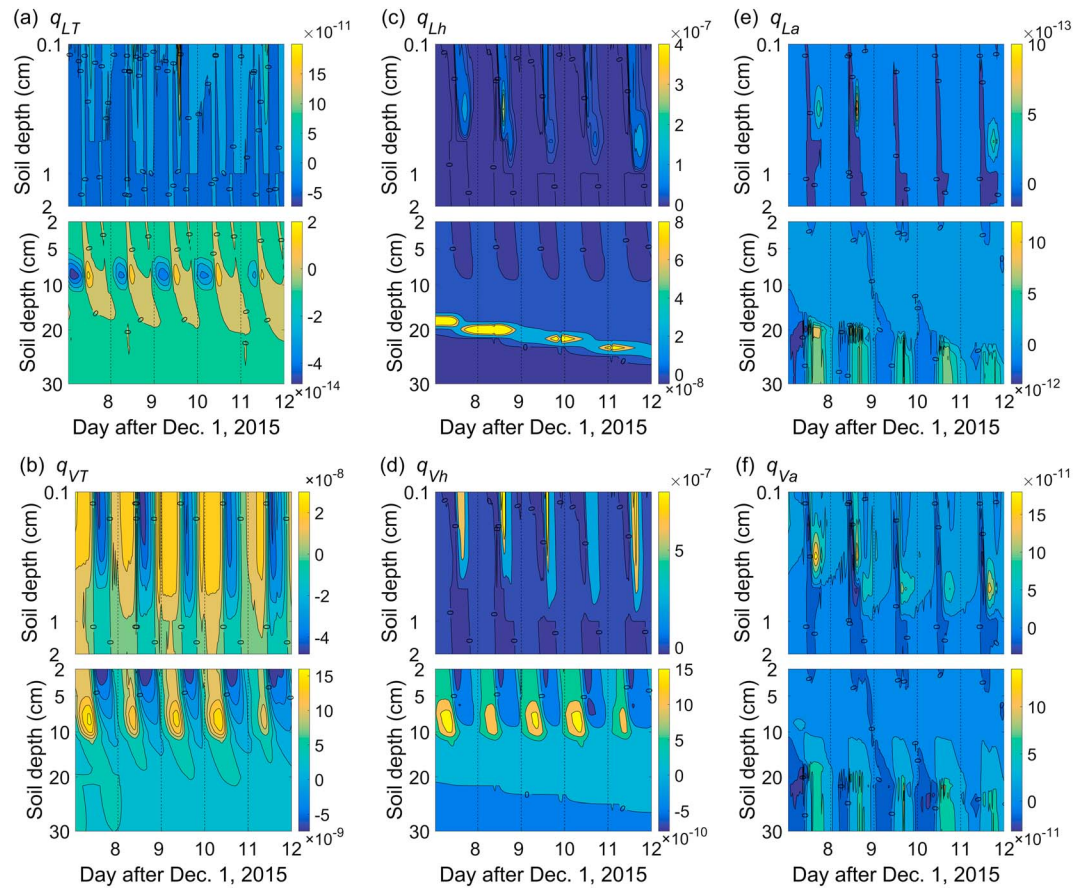
Figure 12. The spatial and temporal distributions of (a and b) thermal liquid water and vapor fluxes, (c and d) isothermal liquid water and vapor fluxes, and (e and f) advective liquid water and vapor fluxes at surface soil layers (top 2 cm, upper figure) and deeper soil layers (2–30 cm, bottom figure), respectively, of a typical freezing period during eighth and twelfth days after 1 December 2015. Note that the unit for the fluxes is $g \cdot cm^{-2} \cdot s^{-1}$.

Figures 11 and 12 show the spatial and temporal distribution of matric potential, temperature, and air pressure gradients and the gradient-induced water/vapor fluxes of a typical freezing period. Note that the variations of soil matric potential gradient at shallow soil layers (0.1–2 cm) differ significantly with that at the deeper soil layers (2–30 cm), with about 3 orders difference in the magnitude (Figure 11b). In order to clearly illustrate what happens below the soil depth of 2 cm, surface soil layers (top 2 cm) and deeper soil layers (2–30 cm) are separately presented to have a detailed illustration of gradient fields and fluxes.

Figure 11a shows that soil temperature gradient experiences a diurnal variation in the subsurface layers (from the surface to the freezing front, about 22–24 cm), with a downward gradient during the daytime (from 10:00 to 20:00) and an upward gradient during the night (from 20:00 to 10:00). This diurnal pattern agrees well with the results of the drying soils (Zeng et al., 2011a). Two points are worth to be mentioned: (i) the difference in the emergence time of downward gradient (10:00 versus 7:30 in Zeng et al., 2011a) is mainly due to the different time zone of two experimental sites and (ii) the region where the diurnal fluctuation of soil temperature gradient, driven by the atmosphere forcing, can be observed as constrained by the freezing front. It implicitly indicates that the influence of the future climate change on the subsurface in cold regions can reach the freezing front. The freezing front, indicating the thickness of active layer, thus can be identified as an important indicator for climate change in cold regions (GCOS, 2015). There were five zero-gradient lines, on which the exchange of heat flux was 0. The gradient was negative above the zero-gradient line while positive below the zero-gradient line, which indicated that the fluxes driven by temperature gradient accumulated around the zero-gradient lines (see Figure 12b). These zero-gradient lines can also indicate the
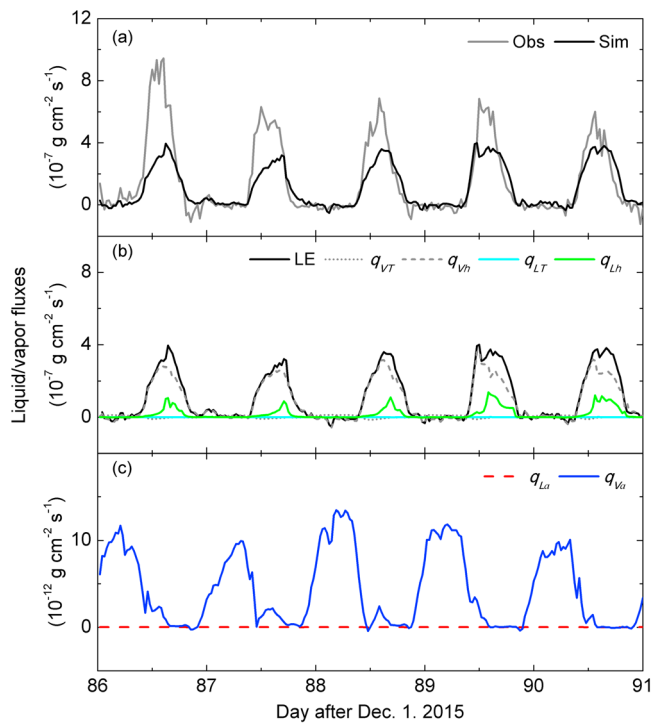
Figure 13. Same as Figure 8 but for a typical five-day thawing period (from 87th to 91th days after 1 December 2015).

position of cold front. At soil depth below the freezing front, the variations of soil temperature were largely reduced and the soil temperature gradient was less than 0.1 °C/cm.

The diurnal patterns of soil matric potential gradient can be recognized from soil surface to the freezing front, and the gradient was positive during the night and negative/less positive during the daytime. The variations of soil matric potential at shallow soil layers (0.1–1 cm) were significantly larger than that at the deeper soil layers (1–24 cm), with about 3 orders difference in the magnitude. Two kinds of zero-gradient lines were identified in Figure 11b:

1. The first kind of zero-gradient lines initialized from the surface and extended vertically to the depth of 8 cm. The soil matric potential gradient was positive outside the zero-gradient lines while negative inside the zero-gradient lines, implying that the fluxes driven by the soil matric potential gradient moved toward and accumulated around the zero-gradient lines at a depth of 8 cm (sink, Figures 12c and 12d). Interestingly, staring from the tenth day after 1 December, the zero-gradient lines were interrupted by a relatively wet soil layer occurred at around 1 cm, which can be attributed to the downward total water fluxes (the sum of water fluxes is negative around the soil depth of 1 cm; see Figure 9a, Zone 3). The isothermal liquid/vapor fluxes accumulated at the upper part (sink) while diffused at the lower part (source) of this wetter soil layer. The wetter soil layer broke the isothermal liquid/vapor fluxes continuity between the top surface and subsurface soil layers and enhanced the upward transport of isothermal fluxes around 1 cm in the following days (Figures 12c and 12d).

2. The other kind of zero-gradient line lay below the freezing front and propagated downward with time. This kind of zero-gradient line formed the source of water fluxes. The matric potential gradient was upward above this zero-gradient line while downward below it. Note that the isothermal liquid fluxes q_{Lh} are determined not only by the gradient (the directions) but also by the conductivities (the magnitude). Thus, when the isothermal liquid fluxes pass through the freezing front, the presence of soil ice significantly reduces the conductivities and further the amount of fluxes are sharply decreased. Therefore, the fluxes move into the freezing front are remarkably larger than the fluxes move out of the freezing front. Then the isothermal liquid fluxes q_{Lh} appear accumulating around the freezing front (Figure 12c). The gradient of soil matric potential was downward and at a magnitude of 10 cm/cm at the soil layers below the freezing front.

Due to the active water phase change at top surface soil layers (above 1 cm), the diurnal variations of soil air pressure gradient are disturbed (Zeng et al., 2011b). At soil depth below 1 cm, the gradient varied diurnally, positive during the daytime, and negative or less positive during the night (Figure 11c). The time delay and reduced amplitude were perceived for deeper soil layers. The zero-gradient lines grew isolated at shallow soil layers (roughly 1–3 cm) during the daytime and at deeper soil layers (roughly below 10 cm) during the night. At shallow soil layers (1–2 cm), the fluxes diffused at the upper part of zero-gradient lines and accumulated at the lower part of zero-gradient lines during the daytime (see Figures 12e and 12f). And the fluxes diffused along with the zero-gradient lines at deeper soil layers (below 12 cm) during the night.

The overall patterns of soil water/vapor transfer in frozen soils, based on our analysis, can be generalized as follows. A continuous isothermal liquid water q_{Lh}, accompanied with a nonnegligible amount of thermal vapor q_{VT}, moves upward to the freezing front (e.g., Figure 9a). Above the freezing front, where soil ice dominated (Zone 2), soil ice blocks most of the water fluxes except for the thermal vapor flux q_{VT}. This temperature gradient-driven vapor flux transfers, from both the top and bottom soil layers, toward the cold front during the daytime while moves upward to the soil surface during the night.

Liquid/vapor fluxes become active until up to the evaporation front (Zone 3) as the diminishing effect of soil ice. During the daytime, liquid water transfers upward by the isothermal liquid water flux q_{Lh} from both the
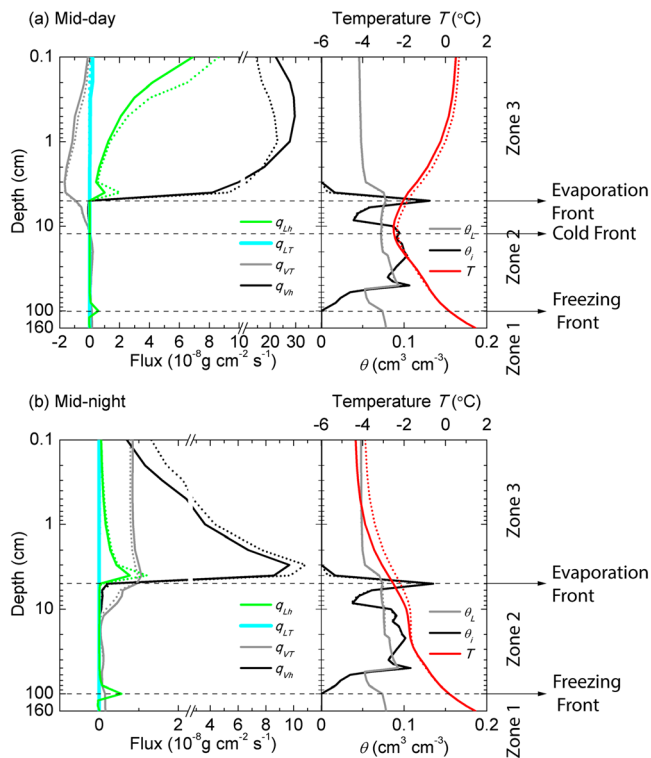
Figure 14. Simulated vertical profiles of the thermal and isothermal liquid water and vapor fluxes, soil ice content at 1200 and 0000 h of a typical freezing period during 90th and 91th days after 1 December 2015. Positive/negative values indicate upward/downward fluxes. The solid lines and dotted lines represent the fluxes and soil moisture, temperature, and ice content profile on the 90th and 91th days after 1 December 2015, respectively.

ice and liquid water phase, partly transforms into water vapor, finally moves toward the surface (Figure 9a). Water vapor directly sublimates from soil ice surface by the isothermal vapor flux q_{Vh} (Figure 9a, Zone 3) and evaporates into the atmosphere as the major flux component. While during the night, thermal vapor flux q_{VT} serves as a continuous source of evaporation (Figure 9b). This diurnal behavior of thermal vapor flux results in the daily cycle of soil moisture in the zone between the evaporation front and cold front. Around the freezing front, water phase experiences a change from liquid/vapor to ice, while at the topsoil layers, the water phase change from ice to liquid/vapor happens due to soil ice melting/sublimation process.

3.3.2. Thawing Period

Figure 13 presents the model performance in simulating latent heat flux during a five-day thawing period. Although the diurnal variations of latent heat flux can be well reproduced by the proposed model, a noticeable underestimation can be observed during the daytime, with the bias of $-4.78E-8$ g · cm^{-2} · s^{-1}. Such an underestimation of latent heat flux can be attributed to two possible reasons. (i) The soil water retention curve/SFCC is of large uncertainty when soil moisture is low. (ii) There was little precipitation (mainly in the form of snow as the air temperature was lower than 0 °C) occurred on the 85th day after 1 December 2015. Thus, the underestimation might be due to the lag effect of snow melting/sublimation, which was simplified in the STEMMUS-FT.

The contribution of flux components to the surface evaporation was similar to the freezing process. The isothermal vapor flux contributed most to the total mass during the daytime, followed by the isothermal liquid flux. Liquid water transferred by the downward thermal vapor flux near the surface was reduced, which is the result of the decrease of the temperature gradient in the top surface layers. The thermal liquid flux, which was small enough to be neglected during the freezing days, was observed upward near the surface when soil began thawing. This behavior was also reported by Saito et al. (2006, Figure 12) when the drying soil experienced the irrigation. The values of air pressure-induced liquid/vapor fluxes are relatively small, and the vertical variations of advective liquid/vapor fluxes are similar to that of freezing periods (results not shown).

Compared to the freezing periods, similar diurnal patterns of water and vapor transport were simulated during the thawing periods (Figure 14). The depth where the upward liquid water occurred was much deeper than the freezing periods. Due to the coarse resolution of vertical profile, there is no difference in the depth of the freezing front between two sequential days. Zone 3 was also extended from about 1 cm in freezing periods to 5 cm in thawing periods as the depletion of soil ice content.

4. Discussion

4.1. The Effect of Soil Ice

When soil experiences the FT process, there is a dynamic coexistence of ice, liquid water, water vapor, and dry air in soil pores. As unfrozen water have been observed not only on the surface of soil aggregates but also among soil ice crystals, the matric potential will be affected by soil ice (Farouki, 1986; Zhang et al., 2007). Thus, the liquid water flow can be driven not only by the moisture gradient but also by the gradient of soil ice content (Zhang et al., 2007), which can be clearly seen in our simulations (e.g., Figure 9 Zone 3). In addition to liquid water, soil ice (sublimation) also serves as the source for the evaporation into atmosphere.

Both experimental and modeling effort have demonstrated that the blocking effect of soil ice exists on the liquid flow passing through a porous medium (Harlan, 1973; Taylor & Luthin, 1978). This effect can be attributed to the ice-induced soil porosity reduction, and the increasing surface contact between solid particles and water. Although an impedance factor was widely employed in models to account for such effect,

some researches pointed out its limitations: (i) not physically based (Newman & Wilson, 1997); (ii) nondifferentiable when soil ice begins to form (Kurylyk & Watanabe, 2013); (iii) constant with varied matric potentials, which has been demonstrated not realistic (Watanabe, 2008; Zhao et al., 2013); and (iv) unable to explicitly take into account the increasing surface contact factor (Koren et al., 2014). Thus, alternative methods to take into account the blocking effect require further research (Azmatch et al., 2012; Kurylyk & Watanabe, 2013; Watanabe & Wake, 2008). In the STEMMUS-FT, the potential-freezing point depression theory and the reversion of water retention equations were combined to derive the SFCC, the parameters of which were further applied in the Mualem hydraulic conductivity scheme to account for the soil ice effect, together with the impedance factor (see equations (A1) and (A2)).

A certain amount of heat can be released/absorbed during FT process. This amount of heat will result in the change of temperature gradient, transformed into thermodynamic moisture potential and then the water pressure gradient (Luo et al., 2003; Romanovsky & Osterkamp, 2000). Then the liquid water flow and vapor flow accumulate toward the freezing front (and diverge around the evaporation front) under the temperature and water pressure gradients. According to the foregoing (Figures 9 and 14), the presence of soil ice constrains the evaporation zone to the depth of 1–5 cm, which is much shallower than that of the drying process (Boulet et al., 1997; Grifoll et al., 2005; Saito et al., 2006). Nevertheless, soil ice serves as the source for evaporation at very top surface layers and the sink for the liquid/vapor water fluxes at the freezing front.

4.2. The Role of Vapor Flow

As both the drying and freezing soils lose liquid water from larger pores to micro ones, it is assumed that the freezing process is, to some extent, similar to the drying process (Dall'Amico, 2010; Hansson et al., 2004; Koopmans & Miller, 1966). At soil surface, isothermal vapor flow indeed contributes most to the total mass flux. Due to the day/night behavior of thermal vapor flow, there is a diurnal variation of moisture content at topsoil layers (Figure 5). Such kind of behavior is similar to that of the drying process reported by Boulet et al. (1997) and Saito et al. (2006). While, the difference is that this vapor circulation can only be restricted in the zone between the soil surface and the cold front during FT process. Vapor flow move upward to the freezing front and contribute about 6%–13% to the total water flux for the ice formation, which agrees well with the results of (Teng et al., 2015; Zhang et al., 2016). The variations in the percentage of vapor flux in the total water flux can be attributed to the interactive effect of moisture gradient field and temperature gradient field (Zhang et al., 2016). The results deduced from our simulations indicate that it is mainly the vapor flow that connects the water/vapor transfer beneath the freezing front (sink) and above the evaporation front (source).

4.3. The Role of Air Flow

Since the natural field experiment is normally considered as an open boundary condition, the variation of air pressure due to the volumetric expansion of ice is smaller than the lab experiment with bounded boundary conditions. The contribution of air pressure-induced liquid/vapor fluxes to the total water mass, based on our simulations, is negligible. Nevertheless, the interactive effect of soil ice and air pressure on the vertical variations of advective liquid/vapor fluxes in frozen soils can still be recognized (see Figure 10, taking the freezing period as an example). Furthermore, the diurnal behavior of air pressure resulted in the vapor circulation mainly in the surface region. According to Wicky and Hauck (2017), the air circulation with atmosphere can result in a significant temperature difference between the lower and the upper part of a permafrost talus slope via the convective heat flux and thus have a remarkable effect on the thermal regime in a talus slope. Zeng et al. (2011a) concludes that the air pressure-induced advective fluxes inject the moisture into the topsoil layers and increase the hydraulic conductivity, then further enhance the soil evaporation after precipitation events. These studies clearly prove that the air flow has the potential to affect the hydrothermal regime of subsurface soils. Here we concentrate only on the interactive effect of soil ice and air on the vertical variations of advective fluxes in frozen soils. Further research studies are necessary to explicitly explain the role of air flow in cold regions from the perspective of hydrological, thermal, and ecological effects.

5. Conclusion

We can conclude, from the intercomparison results of different hydrothermal parameterizations, that there is little difference in simulating soil water content, temperature, and freezing depth between two different

hydraulic schemes. The simulation results with different thermal schemes, however, are significantly different. de Vries parameterization performed better than others in simulating the soil thermal regime. The simplified de Vries method has the potential to be employed over the Tibetan plateau.

The analysis of water and vapor fluxes during FT process indicates that both the liquid and vapor fluxes transfer upward to the freezing front. Due to the blocking effect of ice presence in soil pores, the vapor flow rather than the liquid flow contributes most to the total mass flux in frozen soil region. The diurnal cycle of soil moisture in the zone between the evaporation front and cold front was found mainly due to the diurnal behavior of thermal vapor flux. The isothermal vapor and liquid water fluxes are the major source for the evaporation into atmosphere. The air pressure-induced liquid/vapor fluxes play a negligible role in the total mass transfer. Nevertheless, the interactive effect of soil ice and air can be found on the spatial and temporal variations of water/vapor transfer. Further studies are still essential to investigate the role of dry air flow in cold regions from the multidisciplinary perspective of hydrological, thermal, and ecological effects.

Appendix A

A.1. Unfrozen Water Content

As the fixed freezing point methods are not physically realistic, in this paper, we employed SFCC method to estimate unfrozen water content. In combination with two soil water retention curve models, two different expressions of SFCC are given below:

A.1.1. Clapeyron + van Genuchten

$$\theta_{tot}(h) = \begin{cases} \theta_r + \dfrac{\theta_s - \theta_r}{[1 + |\alpha h|^n]^m}, & h < 0 \\ \theta_s, & h \geq 0 \end{cases},$$ (A1)

where α is related to the inverse air-entry pressure. The θ_{tot}, θ_s, and θ_r are the total water content, saturated water content, and the residual water content, respectively; h (m) is the prefreezing soil water potential; and m is the empirical parameter. The parameter m is a measure of the pore size distribution and can be expressed as $m = 1-1/n$, which in turn can be determined by fitting van Genuchten's analytical model (van Genuchten, 1980).

The unfrozen water content was estimated by employing SFCC (Dall'Amico, 2010)

$$\theta_L(h, T) = \theta_r + \frac{\theta_s - \theta_r}{[1 + |\alpha(h + h_{Frz})|^n]^m},$$ (A2)

where θ_L is the liquid water content, L_f (J/kg) is the latent heat of fusion, g (m/s^2) is the gravity acceleration, T_0 (273.15 °C) is the absolute temperature; h (m) is the prefreezing pressure and α, n, and m are the van Genuchten fitting parameters; h_{Frz} (m) is the soil freezing potential.

$$h_{Frz} = \frac{L_f}{gT_0}(T - T_0) \cdot H(T - T_{CRIT}),$$ (A3)

where T (°C) is the soil temperature. H is the Heaviside function, whose value is zero for negative argument and one for positive argument, T_{CRIT} (°C) is the soil freezing temperature.

$$T_{CRIT} = T_0 + \frac{ghT_0}{L_f},$$ (A4)

A.1.2. Clapeyron + Clapp and Hornberger

$$\theta_L(h, T) = \theta_s \left(\frac{L_f}{g\psi_s} \frac{T - T_f}{T} \right)^{-1/b},$$ (A5)

where ψ_s (m) is the air-entry pore water potential and b is the empirical Clapp and Hornberger parameter (Clapp & Hornberger, 1978).

A.2. Hydraulic Conductivity

According to Mualem (1976), the unsaturated hydraulic conductivity using Clapp and Hornberger, van Genuchten method can be expressed as

$$K_{Lh} = K_s(\theta/\theta_s)^{3+2/\beta}, \tag{A6}$$

$$K_{Lh} = K_s S_e^l \left[1 - \left(1 - S_e^{1/m}\right)^m\right]^2, \tag{A7a}$$

$$S_e = \frac{\theta - \theta_r}{\theta_s - \theta_r}, \tag{A7b}$$

$$m = 1 - 1/n, \tag{A7c}$$

where K_{Lh} and K_s (m/s) are the hydraulic conductivity and saturated hydraulic conductivity, $\beta(=1/b)$ is the empirical Clapp and Hornberger parameter, S_e is the effective saturation; and l, n, and m are the van Genuchten fitting parameters.

The block effect of ice presence is estimated by the impedance factor,

$$K_{fLh} = 10^{-EQ} K_{Lh}, \tag{A8a}$$

$$Q = (\rho_i \theta_i / \rho_L \theta_L), \tag{A8b}$$

where K_{fLh} (m/s) is the hydraulic conductivity in frozen soils, K_{Lh} (m/s) is the hydraulic conductivity in unfrozen soils at the same negative pressure or liquid moisture content, Q is the mass ratio of ice to total water, and E is the empirical constant that accounts for the reduction in permeability due to the formation of ice (Hansson et al., 2004).

A.3. Thermal Conductivity
A.3.1. Johansen Method

$$\lambda_{\text{eff}} = K_e\left(\lambda_{\text{sat}} - \lambda_{\text{dry}}\right) + \lambda_{\text{dry}}, \tag{A9}$$

where the λ_{sat} ($W \cdot m^{-1} \cdot {}^\circ C^{-1}$) is saturated thermal conductivity, λ_{dry} ($W \cdot m^{-1} \cdot {}^\circ C^{-1}$) is the dry thermal conductivity, and K_e is the Kersten number, which can be expressed as (Johansen, 1975)

$$K_e = \begin{cases} \log(\theta/\theta_s) + 1.0, & \theta/\theta_s > 0.05 \\ 0.7 \log\left(\dfrac{\theta}{\theta_s}\right) + 1.0, & \theta/\theta_s > 0.1 \\ \theta/\theta_s, & \text{frozen soil} \end{cases}, \tag{A10}$$

The saturated thermal conductivity λ_{sat} is the weighted value of its components (soil particles λ_{soil} and water λ_{w}),

$$\lambda_{\text{sat}} = \lambda_{\text{soil}}^{1-\theta_s} \lambda_w^{\theta_s}, \tag{A11}$$

While the solid soil thermal conductivity λ_{soil} can be described as

$$\lambda_{\text{soil}} = \lambda_{\text{qtz}}^{\text{qtz}} \lambda_o^{1-\text{qtz}}, \tag{A12}$$

where the λ_{qtz} and λ_o ($W \cdot m^{-1} \cdot {}^\circ C^{-1}$) are the thermal conductivity of the quartz and other soil particles and qtz is the volumetric quartz fraction.

The dry soil thermal conductivity is a function of dry soil density ρ_d,

$$\lambda_{\text{dry}} = \frac{0.135\rho_d + 64.7}{2700 - 0.947\rho_d}, \tag{A13a}$$

Table A.1
Properties of Soil Constituents

Substance	j	λ_j (mcal $\cdot$ cm^{-1} $\cdot$ s^{-1} $\cdot$ °C^{-1})	C_j (mcal $\cdot$ cm^{-1} $\cdot$ s^{-1} $\cdot$ °C^{-1})	ρ_j (g/cm^3)	g_j
Water	1	1.37	1	1	–
Air	2	0.06	0.0003	0.00125	–
Quartz	3	21	0.48	2.66	0.125
Clay minerals	4	7	0.48	2.65	0.125
Organic matter	5	0.6	0.6	1.3	0.5
Ice	6	5.2	0.45	0.92	0.125

Note. de Vries (1963).

$$\rho_d = (1 - \theta_s) \cdot 2700, \tag{A13b}$$

A.3.2. Farouki Method
Similar to Johansen method, the weighted method between the saturated and dry thermal conductivities is utilized by Farouki method to estimate soil thermal conductivity. The difference between Farouki method and Johansen method is to express the dry thermal conductivity and solid soil thermal conductivity as the function of soil texture. Equation can be replaced with (Farouki, 1981)

$$\lambda_{\text{soil}} = \frac{8.80 \cdot (\%\text{sand}) + 2.92 \cdot (\%\text{clay})}{(\%\text{sand}) + (\%\text{clay})}, \tag{A14}$$

where %sand and %clay are the volumetric fraction of sand and clay.

A.3.3. de Vires Method

$$\lambda_{\text{eff}} = \left(\sum_{j=1}^{6} k_j \theta_j \lambda_j\right)\left(\sum_{j=1}^{6} k_j \theta_j\right)^{-1}, \tag{A15}$$

where k_j is the weighting factor for each components, θ_j is the volumetric fraction of the jth constituent, and λ_j (W $\cdot$ m^{-1} $\cdot$ °C^{-1}) is the thermal conductivity of the jth constituent. The six components are (1) water, (2) air, (3) quartz particles, (4) clay minerals, (5) organic matter, and (6) ice (see Table A.1; de Vries, 1963)

$$k_j = \frac{2}{3}\left[1 + \left(\frac{\lambda_j}{\lambda_1} - 1\right)g_j\right]^{-1} + \frac{1}{3}\left[1 + \left(\frac{\lambda_j}{\lambda_1} - 1\right)\left(1 - 2g_j\right)\right]^{-1}, \tag{A16}$$

and g_j is the shape factor of the jth constituent (see Table A.1), of which the shape factor of the air g_2 can be determined as follows,

$$g_2 = \begin{cases} 0.013 + \left(\dfrac{0.022}{\theta_{\text{wilting}}} + \dfrac{0.298}{\theta_s}\right)\theta_L, & \theta_L < \theta_{\text{wilting}} \\[2ex] 0.035 + \dfrac{0.298}{\theta_s}\theta_L, & \theta_L \geq \theta_{\text{wilting}} \end{cases}, \tag{A17}$$

A.3.4. Simplified de Vries Model
Tian et al. (2016) proposed the simplified de Vries method as an alternative method of traditional de Vries method. In this method, the thermal conductivity of soil particles component can be directly estimated based on the relative contribution of measured soil constitutes .

$$\lambda_{\text{eff}} = \frac{\theta_w \lambda_w + k_i \theta_i \lambda_i + k_a \theta_a \lambda_a + k_{\min} \theta_{\min} \lambda_{\min}}{\theta_w + k_i \theta_i + k_a \theta_a + k_{\min} \theta_{\min}}, \tag{A18}$$

where k_{min}, can be derived by equation (A16), is the weighting factor of soil minerals; θ_{min} is the volumetric fraction of soil minerals; and λ_{min} (W $\cdot$ m^{-1} $\cdot$ $\degree$C^{-1}) is the thermal conductivity of soil minerals, can be expressed as the weighted value of its components,

$$\lambda_{min} = \lambda_{sand}^{f_{sand}} \lambda_{silt}^{f_{silt}} \lambda_{clay}^{f_{clay}},$$

(A19)

where f_{sand}, f_{silt}, and f_{clay} are the volumetric fraction of soil sand, silt and clay, respectively. The shape factor of soil minerals is determined as the volumetrically weighted arithmetic mean of the constituent shape factors,

$$g_{a,min} = g_{a,sand} f_{sand} + g_{a,silt} f_{silt} + g_{a,clay} f_{clay},$$

(A20)

where $g_{a,\,sand}$, $g_{a,\,silt}$, and $g_{a,\,clay}$ are the shape factors of soil sand, silt and clay; their values are 0.182, 0.0534, and 0.00775, respectively (Tarnawski & Wagner, 1992; Tarnawski & Wagner, 1993; Tian et al., 2016).

A.4. Gas Phase Density

The gas in the soil pores includes water vapor and dry air. The water vapor density, according to Kelvin's law, is expressed as (Philip & de Vries, 1957)

$$\rho_V = \rho_{sV} H_r, \qquad H_r = \exp\left(\frac{hg}{R_V T}\right),$$

(A21)

where ρ_{sV} is the density of saturated water vapor, H_r is the relative humidity, R_V (461.5 J $\cdot$ kg^{-1} $\cdot$ K^{-1}) is the specific gas constant for vapor, g is the gravitation acceleration, and T is temperature.

Assuming that the pore-air and pore-vapor could be considered as ideal gas, then soil dry air and vapor density can be given as

$$\rho_{da} = \frac{P_{da}}{R_{da} T}, \rho_V = \frac{P_V}{R_V T}$$

(A22)

where R_{da} (287.1 J $\cdot$ kg^{-1} $\cdot$ K^{-1}) is the specific gas constant for dry air; P_{da} and P_V (Pa) are the dry air pressure and vapor pressure. Following Dalton's law of partial pressure, the mixed soil air pressure is the sum of the dry air pressure and the vapor pressure, that is, $P_g = P_{da} + P_V$. Thus, combining with equation (A22), the soil dry air density can be derived as

$$\rho_{da} = \frac{P_g}{R_{da} T} - \frac{\rho_V R_V}{R_{da}}$$

(A23)

References

Azmatch, T. F., Sego, D. C., Arenson, L. U., & Biggar, K. W. (2012). Using soil freezing characteristic curve to estimate the hydraulic conductivity function of partially frozen soils. *Cold Regions Science and Technology*, *83-84*, 103–109. https://doi.org/10.1016/j.coldregions.2012.07.002

Bao, H., Koike, T., Yang, K., Wang, L., Shrestha, M., & Lawford, P. (2016). Development of an enthalpy-based frozen soil model and its validation in a cold region in China. *Journal of Geophysical Research: Atmospheres*, *121*, 5259–5280. https://doi.org/10.1002/2015JD024451

Bittelli, M., Ventura, F., Campbell, G. S., Snyder, R. L., Gallegati, F., & Pisa, P. R. (2008). Coupling of heat, water vapor, and liquid water fluxes to compute evaporation in bare soils. *Journal of Hydrology*, *362*(3), 191–205. https://doi.org/10.1016/j.jhydrol.2008.08.014

Boike, J., Roth, K., & Overduin, P. P. (1998). Thermal and hydrologic dynamics of the active layer at a continuous permafrost site (Taymyr Peninsula, Siberia). *Water Resources Research*, *34*, 355–363. https://doi.org/10.1029/97WR03498

Boone, A. A., & Etchevers, P. (2001). An intercomparison of three snow schemes of varying complexity coupled to the same land surface model: Local-scale evaluation at an alpine site. *Journal of Hydrometeorology*, *2*(4), 374–394. https://doi.org/10.1175/1525-7541(2001)002%3C0374:AIOTSS%3E2.0.CO;2

Boulet, G., Braud, I., & Vauclin, M. (1997). Study of the mechanisms of evaporation under arid conditions using a detailed model of the soil–atmosphere continuum. Application to the EFEDA I experiment. *Journal of Hydrology*, *193*(1), 114–141. https://doi.org/10.1016/S0022-1694(96)03148-4

Burke, E. J., Jones, C. D., & Koven, C. D. (2013). Estimating the permafrost-carbon climate response in the CMIP5 climate models using a simplified approach. *Journal of Climate*, *26*(14), 4897–4909. https://doi.org/10.1175/jcli-d-12-00550.1

Cheng, G., & Wu, T. (2007). Responses of permafrost to climate change and their environmental significance, Qinghai-Tibet Plateau. *Journal of Geophysical Research*, *112*, F02S03. https://doi.org/10.1029/2006JF000631

Clapp, R. B., & Hornberger, G. M. (1978). Empirical equations for some soil hydraulic properties. *Water Resources Research*, *14*, 601–604. https://doi.org/10.1029/WR014i004p00601

Dai, Y., Zeng, X., Dickinson, R. E., & Coauthors (2001). Common Land Model: Technical documentation and user's guide. Retrieved from http://climate.eas.gatech.edu/dai/clmdoc.pdf

Dall'Amico, M. (2010). Coupled water and heat transfer in permafrost modeling. (doctoral dissertation), University of Trento.

Dandar, E., Saaltink, M. W., Carrera, J., & Nemer, B. (2017). A surface model for water and energy balance in cold regions accounting for vapor diffusion. *Hydrology and Earth System Sciences Discussions*, *2017*, 1–25. https://doi.org/10.5194/hess-2016-659

Dente, L., Vekerdy, Z., Wen, J., & Su, Z. (2012). Maqu network for validation of satellite-derived soil moisture products. *International Journal of Applied Earth Observation and Geoinformation*, *17*, 55–65. https://doi.org/10.1016/j.jag.2011.11.004

de Vries, D. A. (1963). *Thermal properties of soils*, (pp. 210–235). Amsterdam: North-Holland Publishing Company.

Ding, B., Yang, K., Yang, W., He, X., Chen, Y., Lazhu, et al. (2017). Development of a Water and Enthalpy Budget-based Glacier mass balance Model (WEB-GM) and its preliminary validation. *Water Resources Research*, *53*, 3146–3178. https://doi.org/10.1002/2016WR018865

Eigenbrod, K., & Kennepohl, G. (1996). Moisture accumulation and pore water pressures at base of pavements. *Transportation Research Record: Journal of the Transportation Research Board*, *1546*, 151–161. https://doi.org/10.3141/1546-17

Endrizzi, S., Gruber, S., Dall'Amico, M., & Rigon, R. (2014). GEOtop 2.0: Simulating the combined energy and water balance at and below the land surface accounting for soil freezing, snow cover and terrain effects. *Geoscientific Model Development*, *7*(6), 2831–2857. https://doi.org/10.5194/gmd-7-2831-2014

Farouki, O. T. (1981). The thermal properties of soils in cold regions. *Cold Regions Science and Technology*, *5*(1), 67–75. https://doi.org/10.1016/0165-232X(81)90041-0

Farouki, O. T. (1986). *Thermal properties of soils, series on rock and soil mechanics*, (Vol. 11, pp. 1–136). Clausthal-Zellerfeld: Trans Tech Publications.

Flerchinger, G. N., & Saxton, K. E. (1989). Simultaneous heat and water model of a freezing snow-residue-soil system. I. Theory and development. *Transactions of the American Society of Agricultural Engineers*, *32*(2), 0565–0571. https://doi.org/10.13031/2013.31040

Garcia Gonzalez, R., Verhoef, A., Luigi Vidale, P., & Braud, I. (2012). Incorporation of water vapor transfer in the JULES land surface model: Implications for key soil variables and land surface fluxes. *Water Resources Research*, *48*, W05538. https://doi.org/10.1029/2011WR011811

GCOS (2015). Status of the Global Observing System for Climate (no. GCOS-195). World Meteorological Organization, Geneva, Switzerland.

Grifoll, J., Gastó, J. M., & Cohen, Y. (2005). Non-isothermal soil water transport and evaporation. *Advances in Water Resources*, *28*(11), 1254–1266. https://doi.org/10.1016/j.advwatres.2005.04.008

Groenevelt, P. H., & Kay, B. D. (1974). On the interaction of water and heat transport in frozen and unfrozen soils: II. The liquid phase1. *Soil Science Society of America Journal*, *38*(3), 400–404. https://doi.org/10.2136/sssaj1974.03615995003800030012x

Hansson, K., Šimůnek, J., Mizoguchi, M., Lundin, L. C., & van Genuchten, M. T. (2004). Water flow and heat transport in frozen soil: Numerical solution and freeze-thaw applications. *Vadose Zone Journal*, *3*(2), 693–704.

Harlan, R. L. (1973). Analysis of coupled heat-fluid transport in partially frozen soil. *Water Resources Research*, *9*, 1314–1323. https://doi.org/10.1029/WR009i005p01314

Hinzman, L. D., Bettez, N. D., Bolton, W. R., Chapin, F. S., Dyurgerov, M. B., Fastie, C. L., et al. (2005). Evidence and implications of recent climate change in northern Alaska and other Arctic regions. *Climatic Change*, *72*(3), 251–298. https://doi.org/10.1007/s10584-005-5352-2

Ishikawa, T., Tokoro, T., & Miura, S. (2016). Influence of freeze–thaw action on hydraulic behavior of unsaturated volcanic coarse-grained soils. *Soils and Foundations*, *56*(5), 790–804. https://doi.org/10.1016/j.sandf.2016.08.005

Jansson, P. E. (2012). CoupModel: Model use, calibration, and validation. *Transactions of the ASABE*, *55*(4), 1337. https://doi.org/10.13031/2013.42245

Johansen, O. (1975). Thermal conductivity of soils, 236 Pp, University of Trondheim.

Koopmans, R. W. R., & Miller, R. D. (1966). Soil freezing and soil water characteristic curves. *Soil Science Society of America Proceedings*, *30*(6), 680–685. https://doi.org/10.2136/sssaj1966.03615995003000060011x

Koren, V., Schaake, J., Mitchell, K., Duan, Q. Y., Chen, F., & Baker, J. M. (1999). A parameterization of snowpack and frozen ground intended for NCEP weather and climate models. *Journal of Geophysical Research*, *104*, 19,569–19,585. https://doi.org/10.1029/1999JD900232

Koren, V., Smith, M., & Cui, Z. (2014). Physically-based modifications to the Sacramento Soil Moisture Accounting model. Part A: Modeling the effects of frozen ground on the runoff generation process. *Journal of Hydrology*, *519*(PD), 3475–3491. https://doi.org/10.1016/j.jhydrol.2014.03.004

Kroes, J., Van Dam, J., Groenendijk, P., Hendriks, R., & Jacobs, C. (2009). SWAP version 3.2. Theory description and user manual Rep., Alterra.

Kurylyk, B. L., & Watanabe, K. (2013). The mathematical representation of freezing and thawing processes in variably-saturated, non-deformable soils. *Advances in Water Resources*, *60*, 160–177. https://doi.org/10.1016/j.advwatres.2013.07.016

Li, X., & Koike, T. (2003). Frozen soil parameterization in SiB2 and its validation with GAME-Tibet observations. *Cold Regions Science and Technology*, *36*(1–3), 165–182. https://doi.org/10.1016/S0165-232X(03)00009-0

Luo, L., Robock, A., Vinnikov, K. Y., Schlosser, C. A., Slater, A. G., Boone, A., et al. (2003). Effects of frozen soil on soil temperature, spring infiltration, and runoff: Results from the PILPS 2(d) experiment at Valdai, Russia. *Journal of Hydrometeorology*, *4*(2), 334–351.

Mualem, Y. (1976). New model for predicting the hydraulic conductivity of unsaturated porous media. *Water Resources Research*, *12*, 513–522. https://doi.org/10.1029/WR012i003p00513

Newman, G. P., & Wilson, G. W. (1997). Heat and mass transfer in unsaturated soils during freezing. *Canadian Geotechnical Journal*, *34*(1), 63–70. https://doi.org/10.1139/t96-085

Oleson, K., Lawrence, D. M., Bonan, G. B., Drewniak, B., Huang, M., Koven, C. D., et al. (2013). Technical description of version 4.5 of the Community Land Model (CLM), NCAR Technical Note NCAR/TN-503+STR, 420 pp. doi:10.5065/D6RR1W7M

Prunty, L., & Bell, J. (2007). Infiltration rate vs. Gas Composition and Pressure in Soil Columns. *Soil Science Society of America Journal*, *71*(5), 1473–1475. https://doi.org/10.2136/sssaj2007.0072N

Qi, J., Vermeer, P. A., & Cheng, G. (2006). A review of the influence of freeze-thaw cycles on soil geotechnical properties. *Permafrost and Periglacial Processes*, *17*(3), 245–252. https://doi.org/10.1002/ppp.559

Romanovsky, V. E., & Osterkamp, T. E. (2000). Effects of unfrozen water on heat and mass transport processes in the active layer and permafrost. *Permafrost and Periglacial Processes*, *11*(3), 219–239. https://doi.org/10.1002/1099-1530(200007/09)11:3%3C219::AID-PPP352%3E3.0.CO;2-7

Saito, H., Šimůnek, J., & Mohanty, B. P. (2006). Numerical analysis of coupled water, vapor, and heat transport in the vadose zone. *Vadose Zone Journal*, *5*(2), 784–800. https://doi.org/10.2136/vzj2006.0007

Scanlon, B. R., & Milly, P. C. D. (1994). Water and heat fluxes in desert soils: 2. Numerical simulations. *Water Resources Research*, *30*, 721–733. https://doi.org/10.1029/93WR03252

Schaefer, K., Lantuit, H., Romanovsky, V. E., Schuur, E. A. G., & Witt, R. (2014). The impact of the permafrost carbon feedback on global climate. *Environmental Research Letters*, *9*(8), 85003. https://doi.org/10.1088/1748-9326/9/8/085003

Su, Z., de Rosnay, P., Wen, J., Wang, L., & Zeng, Y. (2013). Evaluation of ECMWF's soil moisture analyses using observations on the Tibetan Plateau. *Journal of Geophysical Research: Atmospheres*, *118*, 5304–5318. https://doi.org/10.1002/jgrd.50468

Su, Z., Wen, J., Dente, L., van der Velde, R., Wang, L., Ma, Y., et al. (2011). The Tibetan Plateau observatory of plateau scale soil moisture and soil temperature (Tibet-Obs) for quantifying uncertainties in coarse resolution satellite and model products. *Hydrology and Earth System Sciences*, *15*(7), 2303–2316. https://doi.org/10.5194/hess-15-2303-2011

Tarboton, D. G., & Luce, C. H. (1996). Utah Energy Balance Snow Accumulation and Melt Model (UEB), Computer model technical description and users guide, Utah Water Research Laboratory and USDA Forest Service Intermountain Research Station.

Tarnawski, V. R., & Wagner, B. (1992). A new computerized approach to estimating the thermal properties of unfrozen soils. *Canadian Geotechnical Journal*, *29*(4), 714–720. https://doi.org/10.1139/t92-079

Tarnawski, V. R., & Wagner, B. (1993). Modeling the thermal conductivity of frozen soils. *Cold Regions Science and Technology*, *22*(1), 19–31. https://doi.org/10.1016/0165-232X(93)90043-8

Taylor, G. S., & Luthin, J. N. (1978). A model for coupled heat and moisture transfer during soil freezing. *Canadian Geotechnical Journal*, *15*(4), 548–555. https://doi.org/10.1139/t78-058

Teng, J., Zhang, S., Leng, W., & Sheng, D. (2015). Numerical investigation on vapor transfer in unsaturated soil during freezing. *Japanese Geotechnical Society Special Publication*, *1*(3), 29–34. https://doi.org/10.3208/jgssp.CPN-26

Tian, Z., Lu, Y., Horton, R., & Ren, T. (2016). A simplified de Vries-based model to estimate thermal conductivity of unfrozen and frozen soil. *European Journal of Soil Science*, *67*(5), 564–572. https://doi.org/10.1111/ejss.12366

Touma, J., & Vauclin, M. (1986). Experimental and numerical analysis of two-phase infiltration in a partially saturated soil. *Transport in Porous Media*, *1*(1), 27–55. https://doi.org/10.1007/bf01036524

van Genuchten, M. T. (1980). A closed-form equation for predicting the hydraulic conductivity of unsaturated soils. *Soil Science Society of America Journal*, *44*(5), 892–898. https://doi.org/10.2136/sssaj1980.03615995004400050002x

Verseghy, D. (2009). CLASS – The Canadian Land Surface Scheme (version 3.4), climate research division, science and technology branch, Environment Canada.

Viterbo, P., Beljaars, A., Mahfouf, J. F., & Teixeira, J. (1999). The representation of soil moisture freezing and its impact on the stable boundary layer. *Quarterly Journal of the Royal Meteorological Society*, *125*(559), 2401–2426. https://doi.org/10.1002/qj.49712555904

Wang, L., Koike, T., Yang, D., & Yang, K. (2009). Improving the hydrology of the Simple Biosphere Model 2 and its evaluation within the framework of a distributed hydrological model. *Hydrological Sciences Journal*, *54*(6), 989–1006. https://doi.org/10.1623/hysj.54.6.989

Wang, L., Koike, T., Yang, K., Jin, R., & Li, H. (2010). Frozen soil parameterization in a distributed biosphere hydrological model. *Hydrology and Earth System Sciences*, *14*(3), 557–571. https://doi.org/10.5194/hess-14-557-2010

Wang, L., Zhou, J., Qi, J., Sun, L., Yang, K., Tian, L., et al. (2017). Development of a land surface model with coupled snow and frozen soil physics. *Water Resources Research*, *53*, 5085–5103. https://doi.org/10.1002/2017WR020451

Watanabe, K. (2008). Water and heat flow in a directionally frozen silty soil. Paper presented at Proceedings of the third HYDRUS Workshop.

Watanabe, K., & Wake, T. (2008). Hydraulic conductivity in frozen unsaturated soil. Proceedings of the 9th International Conference on Permafrost, 1927–1932.

Wicky, J., & Hauck, C. (2017). Numerical modelling of convective heat transport by air flow in permafrost talus slopes. *The Cryosphere*, *11*(3), 1311–1325. https://doi.org/10.5194/tc-11-1311-2017

Yang, K., Wu, H., Qin, J., Lin, C., Tang, W., & Chen, Y. (2014). Recent climate changes over the Tibetan Plateau and their impacts on energy and water cycle: A review. *Global and Planetary Change*, *112*, 79–91. https://doi.org/10.1016/j.gloplacha.2013.12.001

Yang, Z. L., Yang, Z.-L., Mitchell, K. E., Chen, F., Ek, M. B., Barlage, M., et al. (2011). The Community Noah Land Surface Model with Multi-Parameterization Options (Noah-MP), The University of Texas at Austin, Austin, TX, USA.

Yu, L., Zeng, Y., Su, Z., Cai, H., & Zheng, Z. (2016). The effect of different evapotranspiration methods on portraying soil water dynamics and ET partitioning in a semi-arid environment in Northwest China. *Hydrology and Earth System Sciences*, *20*(3), 975–990. https://doi.org/10.5194/hess-20-975-2016

Zeng, Y. (2013). *Coupled dynamics in soil: Experimental and numerical studies of energy, momentum and mass transfer springer*. Berlin: Springer Theses. https://doi.org/10.1007/978-3-642-34073-4

Zeng, Y., & Su, Z. (2013a). Reply to comment by Binayak P. Mohanty and Zhenlei Yang on "A simulation analysis of the advective effect on evaporation using a two-phase heat and mass flow model". *Water Resources Research*, *49*, 7836–7840. https://doi.org/10.1002/2013wr013764

Zeng, Y., & Su, Z. (2013b). STEMMUS: Simultaneous Transfer of Engery, Mass and Momentum in Unsaturated Soil, University of Twente, Faculty of Geo-Information and Earth Observation (ITC), Enschede.

Zeng, Y., Su, Z., van der Velde, R., Wang, L., Xu, K., Wang, X., & Wen, J. (2016). Blending satellite observed, model simulated, and in situ measured soil moisture over Tibetan Plateau. *Remote Sensing*, *8*(3). https://doi.org/10.3390/rs8030268

Zeng, Y., Su, Z., Wan, L., & Wen, J. (2011a). A simulation analysis of the advective effect on evaporation using a two-phase heat and mass flow model. *Water Resources Research*, *47*, W10529. https://doi.org/10.1029/2011WR010701

Zeng, Y., Su, Z., Wan, L., & Wen, J. (2011b). Numerical analysis of air-water-heat flow in unsaturated soil: Is it necessary to consider airflow in land surface models? *Journal of Geophysical Research*, *116*, D20107. https://doi.org/10.1029/2011JD015835

Zeng, Y., Su, Z., Wan, L., Yang, Z., Zhang, T., Tian, H., et al. (2009). Diurnal pattern of the drying front in desert and its application for determining the effective infiltration. *Hydrology and Earth System Sciences*, *13*(6), 703–714. https://doi.org/10.5194/hess-13-703-2009

Zeng, Y., Wan, L., Su, Z., Saito, H., Huang, K., & Wang, X. (2009). Diurnal soil water dynamics in the shallow vadose zone (field site of China University of Geosciences, China). *Environmental Geology*, *58*(1), 11–23. https://doi.org/10.1007/s00254-008-1485-8

Zhang, S., Teng, J., He, Z., & Sheng, D. (2016). Importance of vapor flow in unsaturated freezing soil: A numerical study. *Cold Regions Science and Technology*, *126*, 1–9. https://doi.org/10.1016/j.coldregions.2016.02.011

Zhang, X., Sun, S. F., & Xue, Y. (2007). Development and testing of a frozen soil parameterization for cold region studies. *Journal of Hydrometeorology*, *8*(4), 690–701. https://doi.org/10.1175/JHM605.1

Zhang, Y., Carey, S. K., & Quinton, W. L. (2008). Evaluation of the algorithms and parameterizations for ground thawing and freezing simulation in permafrost regions. *Journal of Geophysical Research*, *113*, D17116. https://doi.org/10.1029/2007JD009343

Zhang, Y., Carey, S. K., Quinton, W. L., Janowicz, J. R., Pomeroy, J. W., & Flerchinger, G. N. (2010). Comparison of algorithms and parameterisations for infiltration into organic-covered permafrost soils. *Hydrology and Earth System Sciences*, *14*(5), 729–750. https://doi.org/10.5194/hess-14-729-2010

Zhang, Y., Cheng, G., Li, X., Han, X., Wang, L., Li, H., et al. (2013). Coupling of a simultaneous heat and water model with a distributed hydrological model and evaluation of the combined model in a cold region watershed. *Hydrological Processes*, *27*(25), 3762–3776. https://doi.org/10.1002/hyp.9514

Zhao, H., Zeng, Y., Lv, S., & Su, Z. (2018). Analysis of soil hydraulic and thermal properties for land surface modelling over the Tibetan Plateau. *Earth System Science Data Discussions*, 1–40. https://doi.org/10.5194/essd-2017-122

Zhao, H., Zeng, Y., Su, Z. (2017). Soil hydraulic and thermal properties for land surface modelling over the Tibetan Plateau. University of Twente. Dataset. https://doi.org/10.4121/uuid:61db65b1-b2aa-4ada-b41e-61ef70e57e4a

Zhao, Y., Nishimura, T., Hill, R., & Miyazaki, T. (2013). Determining hydraulic conductivity for air-filled porosity in an unsaturated frozen soil by the multistep outflow method. *Vadose Zone Journal*, *12*(1). https://doi.org/10.2136/vzj2012.0061

Zheng, D. (2015). Water and heat exchanges on the Tibetan Plateau: Observation and modeling of the yellow river source region. (Doctoral dissertation), University of Twente.

Zheng, D., van der Velde, R., Su, Z., Booij, M. J., Hoekstra, A. Y., & Wen, J. (2014). Assessment of roughness length schemes implemented within the Noah Land Surface Model for high-altitude regions. *Journal of Hydrometeorology*, *15*(3), 921–937. https://doi.org/10.1175/jhm-d-13-0102.1

Zheng, D., van der Velde, R., Su, Z., Wang, X., Wen, J., Booij, M. J., et al. (2015). Augmentations to the Noah model physics for application to the Yellow River source area. Part I: Soil water flow. *Journal of Hydrometeorology*, *16*(6), 2659–2676. https://doi.org/10.1175/JHM-D-14-0198.1

Zheng, D., van der Velde, R., Su, Z., Wen, J., Wang, X., & Yang, K. (2017). Evaluation of Noah frozen soil parameterization for application to a Tibetan meadow ecosystem. *Journal of Hydrometeorology*, *18*(6), 1749–1763. https://doi.org/10.1175/jhm-d-16-0199.1

Zheng, D., Wang, X., van der Velde, R., Zeng, Y., Wen, J., Wang, Z., et al. (2017). L-band microwave emission of soil freeze-thaw process in the third pole environment. *IEEE Transactions on Geoscience and Remote Sensing*, *55*(9), 5324–5338. https://doi.org/10.1109/TGRS.2017.2705248